Journal of Structural Geology 174 (2023) 104924

Contents lists available at ScienceDirect

Journal of Structural Geology

journal homepage: www.elsevier.com/locate/jsg

Deformation of columnar calcite within flowstone speleothem

Ivanka Mitrović-Woodell [a,*], Telemaco Tesei [b], Lukas Plan [c], Gerlinde Habler [a], Ivo Baroň [d], Bernhard Grasemann [a]

[a] University of Vienna, Department of Geology, Josef Holaubek-Platz 2, 1090, Vienna, Austria
[b] University of Padua, Department of Geosciences, Via Gradenigo 6, 35131, Padova, Italy
[c] Natural History Museum, Karst and Cave Group, Burgring 7, 1010, Vienna, Austria
[d] Institute of Rock Structure and Mechanics, The Czech Academy of Sciences, V Holesovickach 94/41, 182 09, Prague, Czech Republic

ARTICLE INFO

Keywords:
Flowstone speleothem
Calcite
Pulverization
Comminution
Brecciation
Low temperature deformation

ABSTRACT

Damaged and faulted speleothems have proven valuable for neotectonic investigations and dating. Flowstone (or "bacon") speleothems often consist of coarse (cm-scale) columnar calcite with a pronounced primary crystal orientation. However, experimental and microstructural investigations of faulted flowstones are rare. What are the deformation mechanisms in flowstone and how can they be compared to deformation in faulted limestone and marbles is unclear. This study examines deformation mechanisms in flowstone and shows how crystal orientation affects pulverization. Direct shear experiments of columnar flowstone calcite were conducted under room conditions, employing low sliding velocities (1–10 μm/s) and normal stresses (3–10 MPa). The distinctive primary crystal orientation and relatively large crystal size (up to 10 mm) of flowstone allow for an intra- and intercrystalline deformation analysis. The deformation architecture and mechanical strength directly depend on the primary crystal orientation. Mechanical twinning increases in density and thickness, and it accommodates change in crystal orientation. Retrieved samples reveal in-situ pulverization with a drastic grain size reduction, caused by an interplay between mechanical twinning, cleavage and fracture propagation. At relatively small displacements (<10 mm) and strain (0.2) comminution develops a fine gouge. These findings contribute to a better understanding of the behavior of faulted speleothems and their potential implications for neotectonic studies.

1. Introduction

Damaged and faulted speleothems recently became an important subject to study active tectonics (Baroň et al. 2019, 2022; Sala et al., 2022; Szczygieł et al., 2022). Considering that calcitic speleothems are a type of carbonates, deformation processes that have been studied thoroughly in carbonate rocks should apply to faulted speleothem studies. Furthermore, carbonates studies add to the understanding of processes that lead to brittle faulting of the shallow crust, therefore contributing to both earthquake and landslide awareness. Fault slip results in drastic grain size reduction (Balsamo and Storti 2011; Luther et al., 2013), which may occur by pulverization and comminution (Reches and Dewers 2005; Mair and Abe 2011; Fondriest et al., 2015). Rock pulverization in particular is a phenomenon in which a dense network of fractures pervade the rocks without macroscopic strain of the rock, possibly during the early stages of fault rock formation (Fondriest et al., 2015; Schröckenfuchs et al., 2015). Pulverized rocks have been attributed to coseismic fracture propagation since they outcrop at restraining bends of seismic faults and because of the high dynamic loads required to obtain them in the lab (Dor et al., 2006; Doan and Gary 2009; Yuan et al., 2011; Rempe et al., 2013; Fondriest et al., 2015). Comminution progressively develops in the fault core as a consequence of abrasion and particle fragmentation during shear (Sammis et al., 1987; Billi and Storti 2004). Together, these two processes of grain size reduction may be a mechanism or a prerequisite for slip weakening in faults (Monzawa and Otsuki 2003; Storti et al., 2003; Reches and Lockner, 2010; Pozzi et al., 2021). Although pulverization and comminution are sometimes used interchangeably, here we refer to rock pulverization as in-situ crushing with no rotational translation, and grain comminution as abrasive shearing with rotational translation.

Since carbonate rocks are common in the shallow crust and host widespread seismicity (e.g. Chiaraluce et al., 2005, 2017; Bernard et al., 2006; Burchfiel, 2008) calcite mechanical properties have long been studied (Turner and Orozco 1976; Barber and Wenk 1979). To better

* Corresponding author.
E-mail address: ivanka.woodell@gmail.com (I. Mitrović-Woodell).

https://doi.org/10.1016/j.jsg.2023.104924
Received 13 March 2023; Received in revised form 26 July 2023; Accepted 27 July 2023
Available online 3 August 2023

understand and evaluate (paleo)slip conditions, researchers have analyzed microstructures within both natural (Rybacki et al., 2011; Smith et al., 2011; Fondriest et al., 2012; Tesei et al., 2013; Schröckenfuchs et al., 2015) and experimental (Niemeijer et al., 2012; Ree et al., 2014; Tesei et al., 2014, 2017; Verberne et al., 2014; De Paola et al., 2015) shear zones in carbonates. Samples used in these studies covered a wide range of calcitic rocks, from calcite single crystals (Braillon et al., 1978; De Bresser and Spiers, 1993; 1997; Barber et al., 2007; Parlangeau et al., 2019), to marbles (Bestmann et al., 2000; Barnhoorn et al., 2004; Ree et al., 2014), limestones (Smith et al., 2011; Fondriest et al., 2012; Tesei et al., 2014; Verberne et al., 2013, 2014), and dolomites (Barber and Wenk 1979; Barber et al., 2007; Schröckenfuchs et al., 2015). Large calcite crystals with columnar fabric, with preferentially oriented crystals have rarely been studied with respect to shearing behavior, even though they allow to evaluate, at relatively large scale, several poorly investigated aspects of deformation. For instance, in which ways does the orientation of crystals affect the deformation? Faulted speleothems have been used for microstructural analysis rarely, although they can be dated for fault age constraints (Plan et al., 2010, 2019; Sala et al., 2022).

In this study, we investigate deformation processes in natural flowstones composed of calcite crystals with columnar fabric. Flowstone speleothems were chosen as a starting material due to their distinct crystal orientation, large crystal size (up to 1 cm), and their ability to record past faulting events (Plan et al., 2010; Baroň et al., 2022). Direct shear experiments, conducted on calcitic flowstone under room conditions, utilized low sliding velocities (1–10 μm/s) and normal stresses (3–10 MPa). The retrieved samples were analyzed with optical and scanning electron microscopy, including crystallographic orientation mapping. Our findings demonstrate that the strength and deformation style are directly influenced by the primary crystal orientation. We observe significant grain size reduction (from cm-to nm-scale) accommodated by in-situ pulverization and comminution at very small displacement (5–6 mm) and strain (0.2). In-situ pulverization process results from the interplay between mechanical twins, fractures and crystal boundaries. Additionally, comminution can fully develop a fault gouge with Riedel shears with just a few millimeters of slip. It is important to note that "pulverized rocks" observed in our laboratory experiments differ from the large-scale pulverization associated with dynamic shear rupture propagation at intersonic speed (e.g. Freund 1998).

2. Geology

Flowstone samples used in this study were obtained from Hirschgruben cave (UTM 33N: 506987/5272020), Hochschwab karst massif, Austria, located within a branch of the Salzachtal-Ennstal-Mariazell-Puchberg (SEMP) fault zone (Fig. 1a). Hirschgruben cave, with the entrance at 1890 m above sea level, is located 6.7 km south of the SEMP fault core. The sinistral strike-slip SEMP fault zone extends 400 km across the Eastern Alps and, together with the dextral Periadriatic fault, it accommodated the lateral extrusion of the Eastern Alps toward the Carpatho-Pannonian region during Oligocene and Early Miocene (Linzer et al., 2002). However, some brittle faults are currently still active at sub-millimeter scale (Baroň et al., 2019). Evidence of recent tectonic activity is observed within the SEMP fault zone, both inside and around Hirschgruben cave (Fig. 1b, Plan et al., 2010, 2019; Szczygiel et al., 2022). The cave's faulting conditions suggest low temperatures (5 °C),

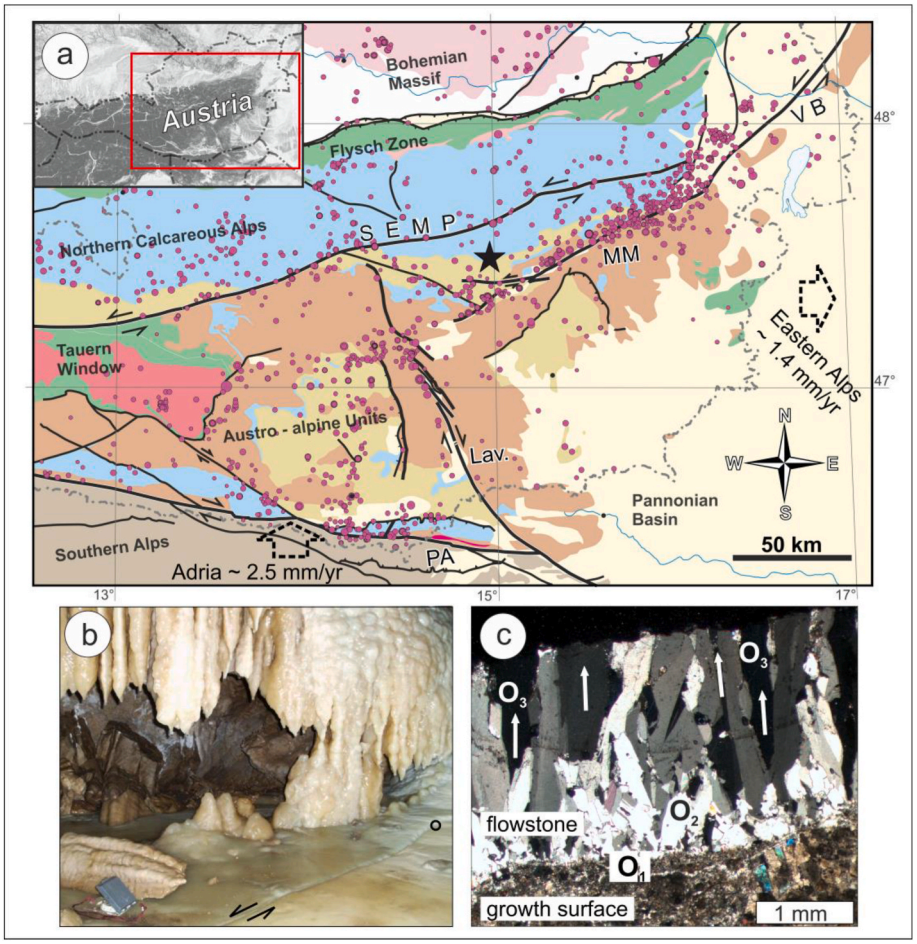

Fig. 1. The Hirschgruben cave:
a. Location of the cave (indicated by a black star) with major fault systems (black lines paired with half-arrows give shear sense) on the geological map of Austria (after Baroň et al., 2019): SEMP—Salzachtal-Ennstal-Mariazell-Puchberg fault, PA—Periadriatic fault, MM—Mur-Mürz fault, Lav. - Lavantal fault, VB—Vienna Basin.
b. A faulted flowstone inside the cave, reported in Plan et al. (2010), was used as a baseline for this study; a pair of half-arrows gives sense of shear; sampling location is marked by a black circle; geologic compass for scale in the lower left corner.
c. XPL micrograph of flowstone growth: white arrows show growth direction, i.e. orientation of the calcite c-axes; note straight and serrated boundaries and uniform extinction of calcite crystals; growth stages are: O1- competitive growth at the base, O2- more favorable orientations with calcite c-axis (sub) perpendicular to the growth surface, O3- perpendicular c-axes are dominant (see text for detailed description); the image is from the same thin section used in Plan et al. (2010).

high relative humidity (95–100%), and vadose conditions, indicating water-unsaturated conditions with minimum water present during the deformation process. Considering that the flowstone formation consists of calcite crystals that grow perpendicular to the growth surface (Figs. 1c and 2a), the flowstone sheared in the cave was oriented with calcite c-axis (long or growth axis) roughly perpendicular to the shear plane.

3. Methods

3.1. Specimen collection and preparation

Two flowstone boulders were collected near the entrance of Hirschgruben cave. They were naturally broken off from the cave walls due to frost weathering. We examined the samples to be pristine, free from impurities (clay and similar) or signs of other deformation. The flowstone boulders (Fig. 2a) were cut into rectangular blocks (Fig. 2b) at the National Institute of Geophysics and Volcanology (INGV), Italy. The blocks, measuring 4 × 8 cm and 4 × 4 cm, were cut either parallel or perpendicular to the calcite c-axes (Fig. 2), allowing us to test the effect of the preferential orientation of the calcite c-axis relative to the fault surface.

The specimens had a layered composition of coarse and fine calcite crystals, typical of speleothem growth, which is described in detail in the following sections. To ensure uniform thickness and minimize artificial stress concentration, the blocks were prepared with a parallel grinder and roughened with P60 sandpaper (particle size ca. 260 μm). A control sample was collected during the preparation process to confirm the absence of penetrative damage related to the preparation steps. Due to the non-uniform orientation of calcite c-axes, a result of the nature of flowstone growth, we did not have control over the absolute crystal orientation prior to the experiments (Fig. 2c,d,e).

3.2. Deformation experiments

Friction experiments were performed using the rock deformation biaxial apparatus (BRAVA, Fig. 3) hosted at INGV, Italy (for further information see Collettini et al., 2014). The experiments were performed in a "single direct" configuration (Fig. 3b,d) at room temperature (ca. 20 °C) and humidity (ca. 56%) conditions. There were two types of the "single direct" configuration: (1) shearing of a single, intact flowstone block ("intact block" hereinafter, Fig. 3b), to test the mechanical behavior of flowstone alone, and (2) shearing a pair of sliding blocks that were sheared against each other (in the text shortened to "bare surface", Fig. 3d), to test the frictional properties of flowstones.

The samples were horizontally secured using two steel forcing blocks, with one side exerting downward pressure to induce shearing. The horizontal piston, operating in load-feedback control mode, provided a constant normal stress, and forces were measured with load cells (±0.03 kN). The horizontal forces were empirically established, with the aim of holding the samples without crushing them. The vertical piston applied a shear displacement on one of the forcing blocks, which transmitted the shearing to the sample. The other side of the forcing block slid against the loading frame via a smooth steel-on-steel interface lubricated with a low-friction Molykote® coating. The vertical piston worked in displacement-feedback control mode, and displacements were measured with linear variable displacement transducer (±0.01 μm precision) attached to each piston.

1. The intact block sliding (Fig. 3a and b) was performed on 40 x 40 × 7 mm samples. The initial loading, with normal stress of 10 MPa, kept constant during the experiment, was followed by the sliding (v = 1–10 μm/s) imposed via the vertical ram. Samples i1 and i10 were oriented to have calcite crystal elongation perpendicular to the sliding direction, and i11 to have calcite crystal elongation parallel to the sliding direction. Total displacement was about 10 mm, with constant sliding velocities of 1 μm/s (i1 and i11) and 10 μm/s (i10).

2. The bare surface tests (Fig. 3c and d) involved shearing a larger specimen block (40 x 80 × 10 mm) against a smaller one (40 x 40 × 10 mm) to maintain constant nominal contact area. Each pair of blocks had sliding surface approximately perpendicular to the bulk of crystal elongation. The normal stress kept constant at 3 MPa, with constant sliding velocities of 1 μm/s (b1) and 10 μm/s (b10), for total displacement of about 5 mm.

Friction was computed as the ratio between the vertical force and the normal force applied by the vertical and horizontal pistons respectively, i.e. $\mu = F_t/F_n$. assuming lack of cohesion.

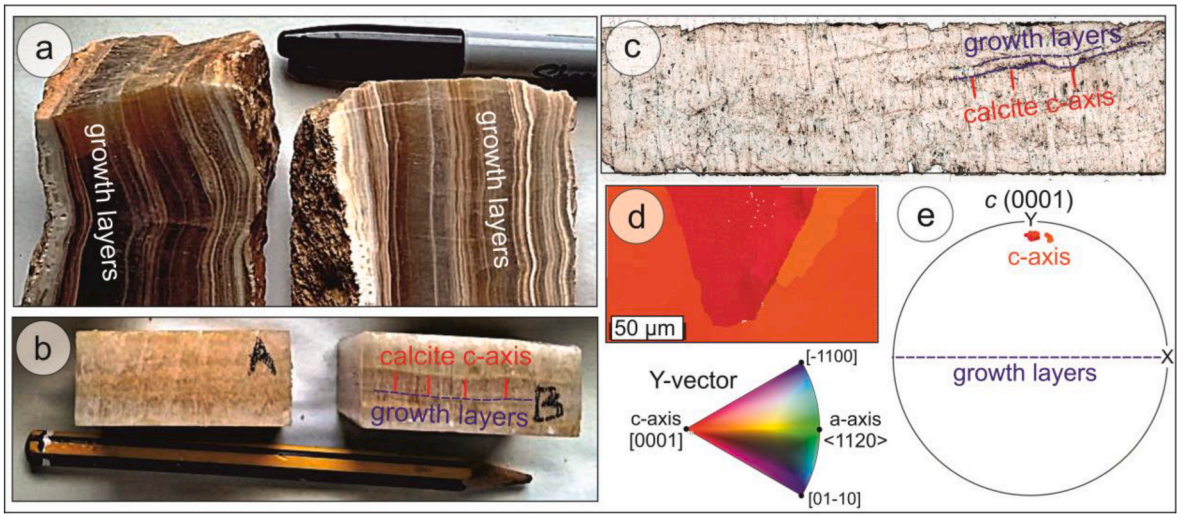

Fig. 2. Flowstone as a starting material:
a. Flowstone boulders used in the study; lines mark growth layers; pen for scale.
b. Flowstone blocks used in experiments, with a sketch of growth layering and the orientation of calcite c-axis (approximately normal to the growth layering); thickness of the block is 1 cm.
c. Thin section **PPL micrograph** of a control sample with a sketch of growth layering and the orientation of calcite c-axis; this sample was prepared for experiments, but not used; pen for scale.
d. EBSD-IPFy colormap showing typical orientation of calcite in flowstone; below the map is an IPFy key with highlighted calcite axes and directions.
e. Equal area projection of calcite c-axes orientations based on the map in (d), (sub)parallel to the Y-vector, and perpendicular to growth layers.

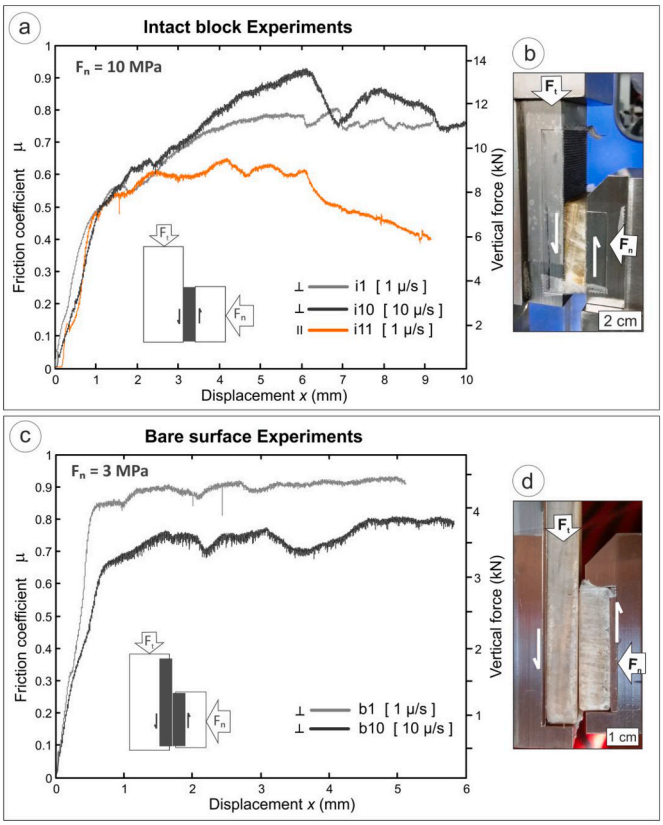

Fig. 3. The BRAVA experiments (at room temperature) with two different experimental configurations, intact (a-b) and bare surface (c-d):
a. Friction coefficient plotted against shear displacement at constant normal stress (10 MPa) and sliding velocity (1–10 μm/s); Inset: a sketch of the experimental set-up.
b. "Intact block" experimental configuration, Fn is normal stress, Ft is shear stress.
c. Friction coefficient plotted against shear displacement at constant normal stress (3 MPa) and sliding velocity (1–10 μm/s); Inset: a sketch of the experimental set-up.
d. "Bare surface" experimental configuration, Fn is normal stress, Ft is shear stress.

3.3. Optical and scanning electron microscopy

After each experiment, samples were carefully retrieved and coated with epoxy, although the fine-grained gouge formed during experiments was difficult to fully preserve. Samples for thin sections were cut perpendicular to the shear plane and parallel to the sliding direction. Thin sections were polished (including the use of colloidal silica slurry Köstrosol 3530), to a thickness of about 25 μm. Initial optical analysis was performed with a Leica DM4500 P optical microscope. Optical micrographs, taken with plane- and crossed-polarized light (PPL and XPL) and standard tint (gypsum) plate, were used for microstructural analyses and selecting the samples for scanning electron microscopy (SEM).

To analyze detailed microstructures developed during experiments, SEM images were collected at the University of Vienna. Electron micrographs were obtained by FEI Inspect S (SEM), combined with Gatan Chroma cathodoluminescence (CL) imaging. The operating conditions for SEM were between 10 and 15 kV accelerating voltage, depending on the magnification, and spot sizes varied around 5–7. Images presented here were acquired using the backscattered electron (BSE) detector in z-contrast mode, where varying gray values mainly reflect variations in chemical composition.

3.4. Crystallographic orientation mapping

Selected samples were analyzed by quantitative crystallographic orientation mapping based on electron backscatter diffraction (EBSD) using the FEI Quanta 3D FEG instrument at the University of Vienna, Department for Lithospheric Research. This instrument was equipped with an EDAX Pegasus Apex 4 system, comprising a Digiview IV EBSD camera and an Apollo XV silicon drift detector for energy-dispersive X-ray spectrometry. The samples were mapped at a stage tilt angle of 70°, and at electron probe settings of 15 kV accelerating voltage and 4 nA probe current. Crystal orientation maps were achieved by beam scanning in square grid mode using a fixed step size between 0.25 and 3.7 μm depending on the crystal and area size. The sample reference frame was parallel to the estimated slip surface.

EBSD data were processed and plotted using the MATLAB© toolbox MTEX 5.1 (Bachmann et al., 2010). Calcite symmetry (see A1 in Appendix) used for calculations was -3m1 (X||a, Y||b*, Z||c*). To clean the data, points with confidence index <0.1, and "grains" smaller than 3 pixels were not considered for further analysis. No "grain dilation" was applied, and the "NotIndexed" points were left as empty space (white in maps). The "grains" larger than 3 pixels were calculated after Bachmann et al. (2011) and used for plotting maps and stereonets. The definition of "grain" in this case refers only to domains with misorientations up to 3°, independent of which part of the crystal these domains belong to. For example, a "grain" that belongs to a single twin lamella will be composed of orientation points bound by the boundaries of the twin (<3°). If the same lamella is cut by another twin or a fracture, the second domain will show as different "grain". Therefore, one twin lamella can be composed of different "grains", and different grains have different numbers of plot points. This is especially important when there is a distribution of orientations within a domain (i.e. "grain").

The default color code for MTEX orientation maps uses inverse pole figure direction (IPF) calculated after Nolze and Hielscher (2016). However, for a better representation of texture, IPF was calculated with respect to the vertical Y vector (IPFy), which is normal to the slip surface, and therefore parallel to the original orientations of the c-axes. The IPFy map was used to show uniformity of the original columnar fabric (red tones), that contrasts deformation fabric (yellow and other tones). For single crystal maps, orientation was represented by local c-axis misorientation map, that shows angles between the local calcite c-axis and a selected reference point. In that case, blue tones show low angle values, and yellow tones highlight up to 90° of change in orientation with respect to the original (growth) orientation. To further explore the change in internal crystal orientation, line profiles bisected crystals, from the original orientation towards the new orientation. The profiles are presented as point-to-origin misorientation profiles.

Equal-area projections show representative crystal orientation in the sample reference plane, using c-axis [0001] and a-axis <11–20>. When representing whole map, stereonets used IPFy color-coding. Specific orientation plots, such as different twin sets vs host, used domain (or "grain") orientations and were given individual colors to highlight the relationships.

Mechanical e-twins were calculated as a rotation about axis <10–14> and angle 78.1030°. Although e-twins are usually described to have three possible twin planes marked with e_1,e_2,e_3, in this work, we use e1, e2, e3 to mark different twin sets. Considering that in some cases it is difficult to say which twin set is older (e1 or e2), we use e1 as the most dominant set, e2 as less dominant or younger twin. Additionally, when younger twins develop within already twinned domain, i.e. "new host" , that twin set is highlighted as e2'.

3.5. Fracture plots

Fracture and twin orientation analysis involved using the Fracpaq MATLAB© toolbox (Healy et al., 2017). Optical and/or electron micrographs were used to create vector files. To mitigate bias, positions of

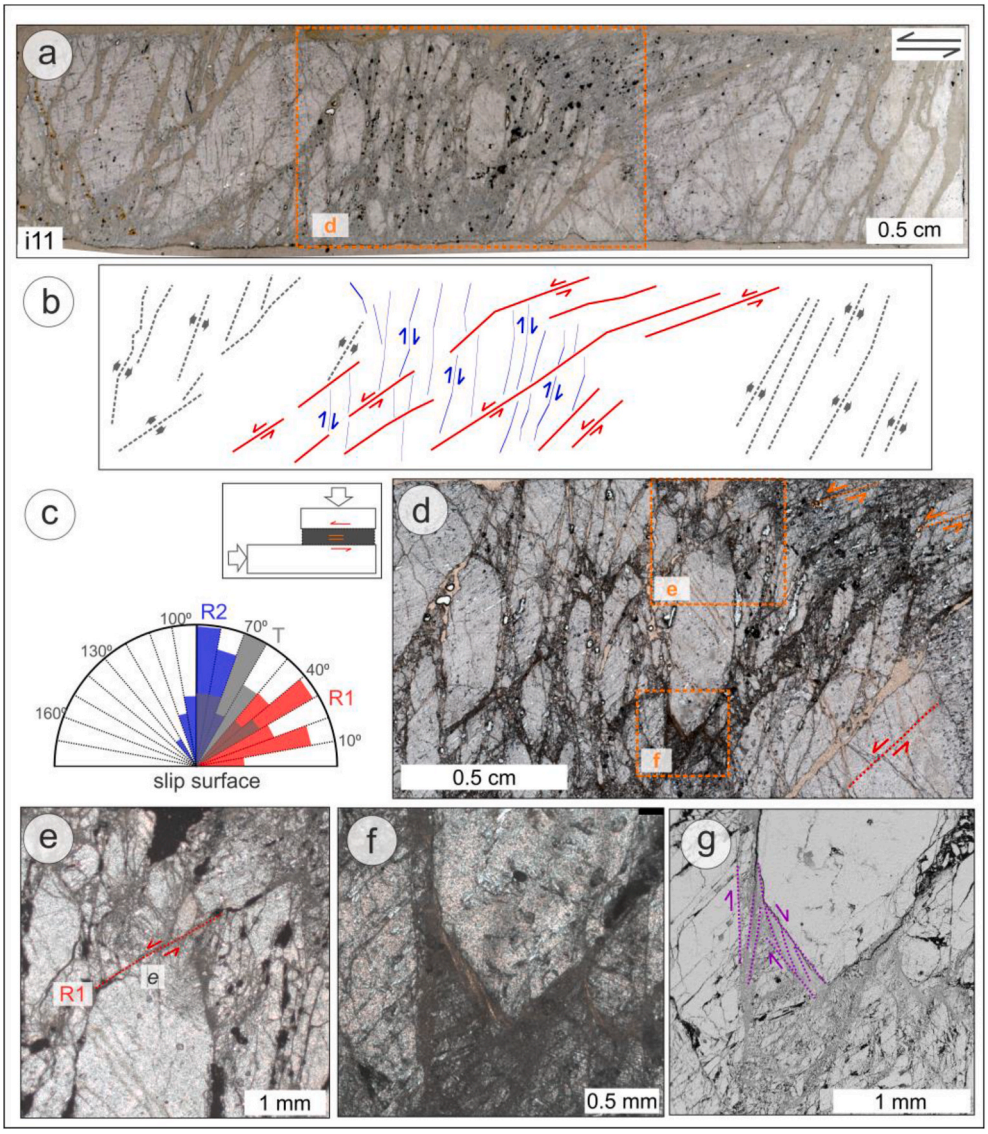

Fig. 4. Retrieved microstructures of the sample i11 (intact block), sheared with calcite c-axes subparallel to the sliding direction, at 1 μm/s:
a. Thin section XPL micrograph shows deformation by intense fracturing; the relative (sinistral) shear direction is marked with half-arrows; orange box marks the position of the image (d).
b. A sketch of interpreted microstructures: synthetic R1 shears [red], antithetic R2 shears [blue], tension fractures T [gray]; note that Riedel shears developed mostly in the central part of the sample, and tension fractures on the sides (due to the proximity of free surfaces).
c. A rose diagram after the sketch in (b) shows the orientations of the representative microstructures with respect to the sliding surface; inset shows a sketch of the experimental configuration.
d. Thin section XPL micrograph of the central area of the sample; orange boxes mark the positions of the images (e, f); synthetic R1 shear [red] offsets growth layers; note sliding along crystal boundaries in the upper right corner [orange].
e. XPL micrograph shows synthetic R1 shear and mechanical e-twins at the tips of the block; note that this is a rare occurrence of mechanical twinning in this sample.
f. XPL micrograph shows fine-grained, gouge material, marked by light-colored bands, localized along the edges of a larger block; the larger block serves as a wedge that creates a dextral shear zone within sinistral shearing of the whole sample.
g. BSE micrograph of the area in (f) shows the geometry of fracture sets [purple] relative to the right-lateral sense of shear, caused by the wedge-effect of the larger block, and localizing the gouge material. (For interpretation of the references to color in this figure legend, the reader is referred to the Web version of this article.)

fractures and twin boundaries were manually extracted with care. Thicker twins were represented by a single line to avoid favoring wider over thinner twins. Rose diagrams were generated from the exported vector files using Fracpaq, employing a 10° segmentation and an equal area projection. However, rose diagrams only represent typical orientation of traces of fractures, cleavage, twin boundaries, and crystal boundaries with respect to the slip surface (here shown as a horizontal line). They do not support detailed statistical analysis. For brevity, the trace orientations are described as "counterclockwise with respect to the trace of the sliding/slip surface" and will be further abbreviated to "cc-ss". The terminology for Riedel shear fractures is color-coded to facilitate representation and incorporates synthetic R1 and P shears, along with antithetic R2 and X shears (equivalent to R′ and P′ shears, respectively) following Logan et al. (1979). To distinguish crystallographically preferred orientations, we use "italic" forms: *cl.* for cleavage {**10-14**}, *e* for twins {01–18}, and *cb.* for long crystal boundaries (parallel to c-axis).

4. Sample primary structure: the nature of flowstone growth

Interpretations of speleothem deformation may be confounded by the nature of speleothem growth because speleothems are composite crystals formed by individual crystallites or subgrains (Kendall and Broughton 1978). Flowstone precipitation occurs when thin water films flow over the growing speleothem surface at rates of 10–100 μm/year (Fairchild et al., 2006), resulting in distinct fabric types and growth layering (Fig. 2a–c). Initially, during flowstone formation (O1 in Fig. 1c), small crystals aggregate and inherit substrate orientation. Subsequent growth stages (O2 in Fig. 1c) involve fewer crystals and a preference for crystallographic orientations normal to the substrate surface (Kendall and Broughton 1978; Broughton 1983). Crystals aligned perpendicular to the interface, with the fastest growth-vector parallel to the calcite c-axis, are favored (Dickson 1993). In later stages (O3 in Fig. 1c), crystals meet along planes without compromising crystal boundaries (Kendall and Broughton 1978). This growth mechanism can produce curved crystals with undulose extinction, as crystals adjust to more favorable orientations at higher angles to the growth surface (Fig. 2e). Flowstone typically has low intergranular porosity (Lindgren et al., 2013).

Flowstone precipitated in karstic caves commonly consists of calcite in a variety of forms and sizes. Our samples show two common fabric types: columnar and micritic (C and M, respectively, Fig. 5a, classification after Frisia et al., 2000, 2014). Columnar fabric consists of large crystals (mm-cm) normal to the growth surface, with elongated calcite columns parallel to the c-axis. Crystal length-to-width ratio is typically ≤6, occasionally with larger values (Fig. 6b). Boundaries between

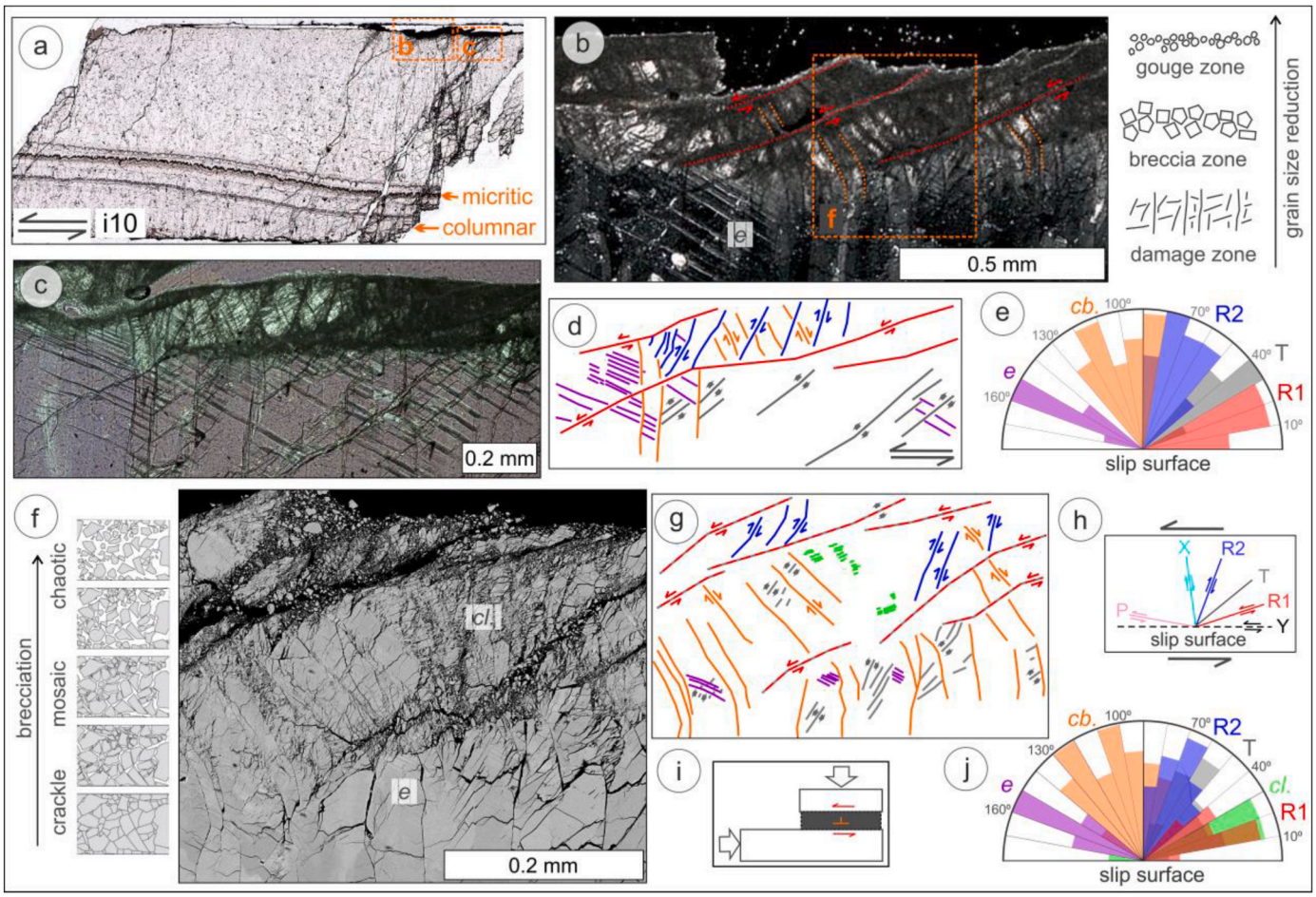

Fig. 5. Retrieved microstructures of the sample i10 (intact block), sheared with c-axes perpendicular to the sliding direction, at 10 μm/s:
a. Thin section image (PPL) shows tension fracture on the sides, but localized bulk of deformation along the upper edge; speleothem micritic and columnar fabric is marked; orange boxes mark the positions of the images (b and c); the relative, left-lateral, shear direction is marked with half-arrows; the sample is 1 cm thick.
b. XPL micrograph shows continuous simple shear marked by crystal-plastic bending (undulose extinction), brecciation, mechanical e twinning and gouge material; microstructural interpretation inside of the micrograph: synthetic R1 shears [red], bent crystal boundaries [orange]; microstructural interpretation on the left side of the micrograph: damage, breccia and gouge zones as compared with those proposed by Billi (2005) and their effect on the increasing grain size reduction; the orange box marks the positions of image in (f).
c. XPL + gypsum micrograph shows bookshelf-faulting, mechanical twinning with increasing intensity towards the edge, and the drastic grain-size reduction.
d. A sketch of the area in (c) with microstructural interpretations: synthetic R1 shears [red], antithetic R2 shears [blue], tension fractures T [gray], long crystal boundaries [cb., orange], mechanical e-twins [e, purple].
e. A rose diagram after the sketch in (d) shows representative orientations with respect to the slip surface; note that the range in orientations of long crystal boundaries reflects the bending, and therefore has two maxima (original and bent).
f. BSE micrograph shows detailed microstructures: e-twins, cleavage, gouge with large tension fractures (open space in black); microstructural interpretation on the left side of the micrograph: progressive brecciation as compared with those proposed by Mort and Woodcock (2008).
g. A sketch of the area in (f) with microstructural interpretations: synthetic R1 shears [red], antithetic R2 shears [blue], tension fractures T [gray], long crystal boundaries [cb., orange], mechanical e-twins [e, purple], cleavage [cl., green].
h. The theoretical geometry of fracture sets relative to the left-lateral sense of shear (after Logan et al., 1979).
i. A sketch of the experimental configuration.
j. A rose diagram after the sketch in (g) shows representative orientations with respect to the slip surface; as in (e), two crystal boundaries maxima correspond to pre- and post-bending orientations. (For interpretation of the references to color in this figure legend, the reader is referred to the Web version of this article.)

crystals may be straight or serrated, and the crystals exhibit uniform extinction and a low density of defects (Fairchild et al., 2006). Micrite fabric comprises small crystals (μm to mm size) arranged in a clotted structure, observed in thin growth layers (<1 mm, Fig. 2a and 5a). Micritic fabric appears dark brown in cross-polarized light (XPL) and dark in plain-polarized light (PPL).

Optical cathodoluminescence microscopy revealed black images for all flowstone samples, indicating the absence of impurities causing fluorescence (e.g. organic matter). The EBSD maps of non-deformed areas show uniform crystal orientation within each crystal, with stereonets confirming the perpendicular c-axis orientation to the slip surface (Figs. 2 and 6). No twins were observed in samples prior to experiments (Fig. 2).

5. Results

5.1. Frictional strength of flowstone

The apparent friction coefficient, calculated with the Amonton's law ($\mu = F_t/F_n$), is plotted on Fig. 3, against shear displacement (x) for each experimental configuration. During each experiment, stress initially showed non-linear increase (Fig. 3), due to compaction and adjustment of sliding surfaces, followed by a linear increase corresponding to the apparent elastic loading of the sample. After the linear stress increase all

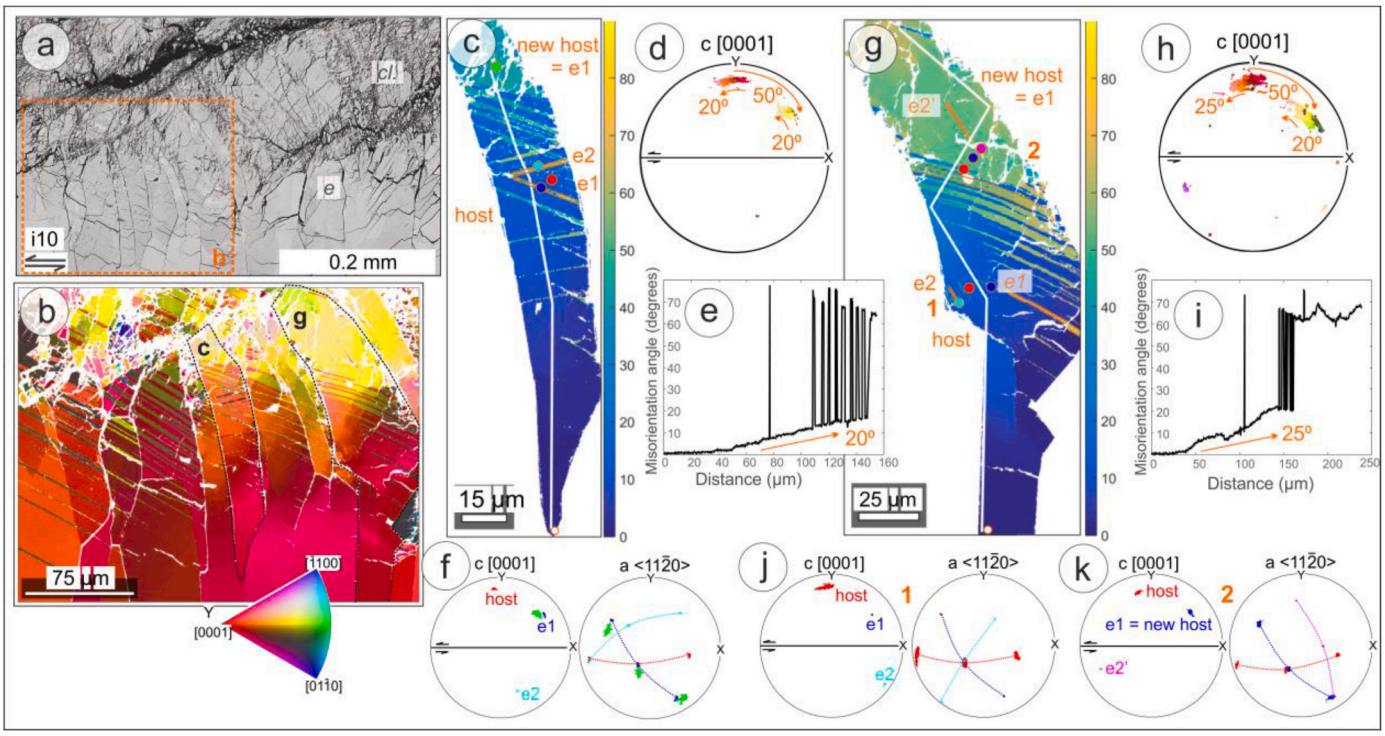

Fig. 6. Crystallographic orientation maps of sample i10 (intact block), c-axis orientation perpendicular to the slip surface:
a. BSE micrograph shows detailed microstructures: e-twins, cleavage, gouge, large tension fractures[black]; orange box marks the positions of EBSD scan area shown in (b); slip surface is located at the top.
b. EBSD -IPFy colormap shows different deformation styles: twins increase in density and thickness, and further accommodate change in orientation of crystals: red tones represent vertical orientations (parallel to Y vector, but perpendicular to slip surface) and yellow tones represent oblique orientations; traced crystals are shown in (c) and (g).
c. Local c-axis misorientation map of a single crystal shows angles between local calcite c-axis and the selected reference point (marked by a white circle at the bottom): c-axis orientations at the top are at about 50° relative to the bottom; white line that bisects the map is a profile line plotted in (e); twins shown in (f) are highlighted with orange lines, and marked original and new host orientations; red, blue and cyan circles are domain orientations plotted in (f), color-coded.
d. Equal-area projections shows c-axes orientations of all points in the crystal in (c), colored by IPFy values (as in (b)); numbers and arrows highlight the angles and directions of internal rotations (20°) and apparent jump/shift caused by twinning (~50°); horizontal line marks relative position of the slip surface (parallel to X vector); note that the internal rotations are gradual and in counterclockwise direction, but the twinning "jump/shift" is in clockwise direction.
e. The misorientation profile (point-to-origin) of the profile line in (c) shows the gradual change in orientations of up to 20°, that concurs with internal rotations shown in (d); higher values (78°) are typical e-twin misorientation angles.
f. Equal-area projections show c- and a-axis orientations of domains marked by points in (c), color-coded; c-plot interprets orientations of host, e1 and e2; a-plot highlights the relationships between the host and two twin sets: each set shares one a-axis with the host.
g. Local c-axis misorientation map of a single crystal shows angles between local calcite c-axis and the selected reference point (marked with a white circle at the bottom): c-axis orientations at the top are at about 50–70° relative to the bottom; a white profile line is plotted as a point-to-origin misorientations profile in (i); e1 and e2, and a younger e2′ twin sets are highlighted with orange lines; original and new host orientations are noted; two sets of domains (sets of three points marked with numbers) are plotted as stereonets in (j) and (k), color-coded; note curved twins in the middle.
h. Equal-area projection shows c-axes orientations of all points in the crystal in (g), colored by IPFy values (as in (b)); numbers and arrows highlight the angles and directions of internal rotations (20–25°) and apparent jump/shift caused by twinning (~50°); horizontal line marks relative position of the slip surface (parallel to X vector); note that the internal rotations are gradual and in counterclockwise direction, but the twinning "jump/shift" is in clockwise direction.
i. The misorientation profile (point-to-origin) of the profile line in (g) shows the gradual change in orientations of up to 25°, that concurs with internal rotations shown in (h); higher values (78°) are typical e-twin misorientation angles.
j. Equal-area projections show c- and a-axis orientations of the first set (1) of domains marked by points in (g), color-coded; c-plot interprets orientations of host, e1 and e2; a-plot highlights the relationships between the host and two twin sets: both sets share the same a-axis with the host, but are rotated about 50° in different directions: older e1 in clockwise, e2 in an apparent counterclockwise direction.
k. Equal-area projections show c-axes and a-axis orientations of the second set (2) of domains marked by points in (g), color-coded; c-plot interprets orientations of host, first twin set e1 and second twin set e2'; however, considering that the crystal adopts the e1 orientation as new host orientation, the second twin set is a twin to the new host [blue]; a-plot highlights the relationships of the original host [red] and the first twin set e1 [blue], and of the new host [blue] and the second twin set e2' [magenta]; note that e2′ and the original host do not share an a-axis. (For interpretation of the references to color in this figure legend, the reader is referred to the Web version of this article.)

samples yielded, and stress/friction further evolved in a complex fashion.

In "intact block" experiments, the overall apparent friction (μ) of the samples with calcite c-axes oriented approximately perpendicular to the sliding surface (samples i1, i10 on Fig. 3a) is consistently higher than 0.7, with peak friction $\mu > 0.9$. The yield point has a similar value at about 0.5–0.55 (Fig. 3a), generally corresponding to the shear stress of 5–5.5 MPa. These samples show gradual slip strengthening within the first 6 mm of shear displacement, followed by slip weakening (Fig. 3a).

Sample i1 (gray line in Fig. 3a), with calcite c-axes oriented approximately perpendicular to the sliding direction, deformed by a sliding velocity of 1 μm/s, has a slight drop of friction ($\Delta\mu = 0.1$) to gradually increase in strength with slip and reach a flat friction coefficient maximum of ca. 0.8 at 7 mm of displacement. In the last 2 mm of

displacement, the frictional strength became steady at 0.7–0.8.

Sample i10 (black line on Fig. 3a), with calcite c-axes oriented approximately perpendicular to the sliding direction, deformed by sliding velocity of 10 μm/s, shows a blunt yield point and immediate slip strengthening, gradually reaching peak friction of 0.9 at 6 mm of shear displacement. A strong decrease in strength (μ is ca. 0.75 at 7 mm of displacement) is followed by the second friction maximum of ca. 0.85 at 8 mm, to become steady slip weakening at ca. 0.75. Throughout the experiment high "noise" was registered, characterized by stress drops in the friction curve. This noise can be interpreted as high-frequency/low-amplitude stick-slip events (periods of intermittent movement "slip" and non-movement "stick").

Sample i11 (orange line in Fig. 3a) with calcite c-axes oriented approximately parallel to the sliding surface, deformed by sliding velocity of 1 μm/s, has a significantly lower friction coefficient, with a maximum of 0.65. The yield point is followed by irregular slip strengthening, with a peak friction coefficient of 0.65 at 4 mm of displacement. At $\mu = 0.6$ and $x = 6$ mm, the frictional behavior drastically changes to gradual slip weakening, with a friction coefficient progressively decreasing down to $\mu = 0.4$ at the end of the experiment.

In "bare surface" experiments, the pairs of blocks were oriented with the calcite c-axis approximately perpendicular to the sliding (bare) surface, at constant normal stress of 3 MPa. Despite different sliding velocities, the overall frictional strength behavior was very similar in both experiments (Fig. 3c): after rapid, nearly linear loading in the first 0.8 mm of displacement, apparent yield marks gradual slip hardening with very few vertical fluctuations.

Sample b1 (gray line on Fig. 3c), deformed by sliding velocity of 1 μm/s, shows a gradual increase in strength with slip, characterized by flat plateaus cut by local minima within first 3 mm of displacement, until achieving steady-state sliding. The peak friction coefficient of 0.9 is achieved at 5 mm of displacement.

Sample b10 (black line on Fig. 3c), deformed by a sliding velocity of 10 μm/s, has irregular and noisy slip strengthening behavior, with local peaks and troughs, until it achieves steady-state sliding at $\mu = 0.8$ and $x = 4.5$ mm. The peak friction coefficient is reached during the steady-state sliding, with $\mu = 0.8$ at 5.5 mm of displacement. Sliding was accompanied by a stick-slip behavior and an increase in layer thickness (see A2 in Appendix).

5.2. Retrieved microstructures

Flowstone samples were sheared at room temperature, relatively low normal stress, 3 and 10 MPa, and sliding velocities, 1 and 10 μm/s. The main deformation mechanisms were brittle fracturing and mechanical twinning, resulting in drastic grain size reduction via both pulverization and comminution. All studied samples developed tensional fractures (ca. 60°cc-ss) during experiments. Along those fractures, samples were chipped off and some of the material was lost.

The edges of the samples were affected by holder grooves (0.1 mm) from the steel holders that held the sample during the experiment (see A3 in Appendix). The grooves induce thin cataclasitic layer and likely aid the localization of slip zones at the sample boundaries, leaving the bulk of the sample as a low-strain zone (A3 in Appendix).

5.2.1. Intact block experiments

Intact block experiments were set up to test the shearing mechanism of flowstone itself. Specimens were positioned either with calcite c-axis (sub)perpendicular (samples i1 and i10), or (sub)parallel (i11) to the slip surface. Microstructural analysis revealed a significant difference in deformation architecture that directly depends on the initial orientation of calcite crystals.

The sample i11 is fractured throughout the sample, with densely spaced tension and shear fractures (Fig. 4a). Tension fractures are localized at the tails of the sample, at ca. 60° cc-ss (Fig. 4b), and their formation is assisted by nearby free surfaces. Synthetic Riedel shears R1 affect the center of the sample and local domains of fine-grained material. R1 shears display two distinct orientations (Fig. 4c): a higher angled (30–40°) cutting through the sample, and a lower angled (10–20°) within finer-grained gouge (Fig. 4a and b). The orientation of the first family of Riedels is very similar to theoretical T orientations (Fig. 4c) to link tensional cracks and low-angle Riedel shears. Antithetic Riedel shears R2 cluster at about 80°cc-ss (Fig. 4c), and together with R1 form block fragments (Fig. 4d). These blocks, or lozenges, elongate parallel to the loading direction. Within the lozenges, the larger blocks are less deformed, and a very-fine grained gouge material is localized along the edges of the larger fragments (Fig. 4f). Fig. 4g shows an antithetic shear zone. This fine-grained material appears shiny in XP light (Fig. 4f). Preexisting intergranular boundaries in flowstone facilitate the fracturing process and induce a bookshelf-like pattern of slipping (Fig. 4d,f). Deformation twins are infrequent and primarily found in the central region of the sample, affecting tips of larger blocks (Fig. 4e).

Contrary to i11, samples with crystals with their c-axes and elongation direction perpendicular to the sliding surface (i1, i10, Fig. 3b) mostly preserved the initial form (Fig. 5a). Despite fractured and chipped off edges of the samples (along tension fractures at 40–60° cc-ss), the bulk of the samples kept the original form (Fig. 5a). Sample i1, sheared at 1 μm/s, has a more distributed deformation style with prominent tension fractures and larger broken fragments, compared to the sample i10, sheared at 10 μm/s. While strain localized at the edges of both samples, the deformation in i10 was considerably more complex, evidenced by intricate patterns of mechanical twinning, bookshelf faulting, and crystal bending (Fig. 5b and c). Therefore, only sample i10 is graphically presented.

The overall deformation intensity ranges from undeformed to highly deformed flowstone towards the top and bottom, associated with increasing grain size reduction (Fig. 5b,c,f). Transitions from undeformed to highly deformed areas appear dark and cloudy in the optical microscope (see the edges in Fig. 5a). The deformation progresses from zones characterized by the presence of mechanical twins and scarce fractures (termed the damage zone, after Billi 2005), to more intense brecciation, with densely spaced and thicker twin lamellae, and undulose extinction (brecciation zone), ultimately to fine-grained gouge with Riedel shears (gouge zone), all within 1 mm from the edge of the sample (Fig. 5b and c).

The *damage zone* typically has tension fractures and thin, widely spaced, twin lamellae. At XP light no change in orientation of primary crystals is observed, as confirmed by orientation maps (Fig. 6). Some crystals display tension fractures only on one side, spreading in a radial pattern (Fig. 5f,6a).

The *brecciation zone* exhibits a higher portion of both breccia and e-twins, compared to the damage zone. Fig. 5f shows that the brecciation pattern, within a single crystal, ranges from crackle to mosaic and chaotic breccia (terminology after Mort and Woodcock, 2008). Fragments are angular and their size varies significantly. Fig. 5f and 6a show large crystals pulverized in-situ, with limited (or no) rotation or translation of the broken fragments. Crystal boundaries act as antithetic X shears (Fig. 5d,g), and cleavage aligns with R1 shears (Fig. 5j).

Density and thickness of twin lamellae increases towards the slip surface (Fig. 5b,c, 6b). Crystals mostly develop one set of twins (Fig. 5c and 6b), though up to three different sets of twins have been observed (e.g. Fig. 6g). Twins start as single straight lamellae, but become thicker (up to ca. 35 μm) and/or curved (Fig. 6b,g). The dominant twin set, e1, is perpendicular to the loading direction, at 150–160° cc-ss (Fig. 5e,j). It accommodates the change in orientation of crystals (Fig. 6): at the bottom of the crystal its c-axis is perpendicular to the slip surface, whereas through twinning, the top of the crystal is rotated 50° clockwise, with respect to the slip surface, and consistent with the overall sinistral sense of shear. This shift in orientation can be seen both in local c-axis misorientation maps (Fig. 6c,g) and equal-area projections (Fig. 6c,g; for easier visualization, also see A4 in Appendix). The second

twin set, e2, has more complex relationships with the host and the first set of twins, either co-existing with e1 (Fig. 6c) or developing in a different area of the crystal (Fig. 6g). The variations in relationships can be compared in stereonets in Fig. 6f and j, where both e1 and e2 share one a-axis with the host, either the same or a different one. However, due to the change in crystal orientation, from the original host position to the e1, a younger twin set, e2′, develops using e1 as a new host (Fig. 6g). This is best visualized in Fig. 6k, where e2' shares an a-axis

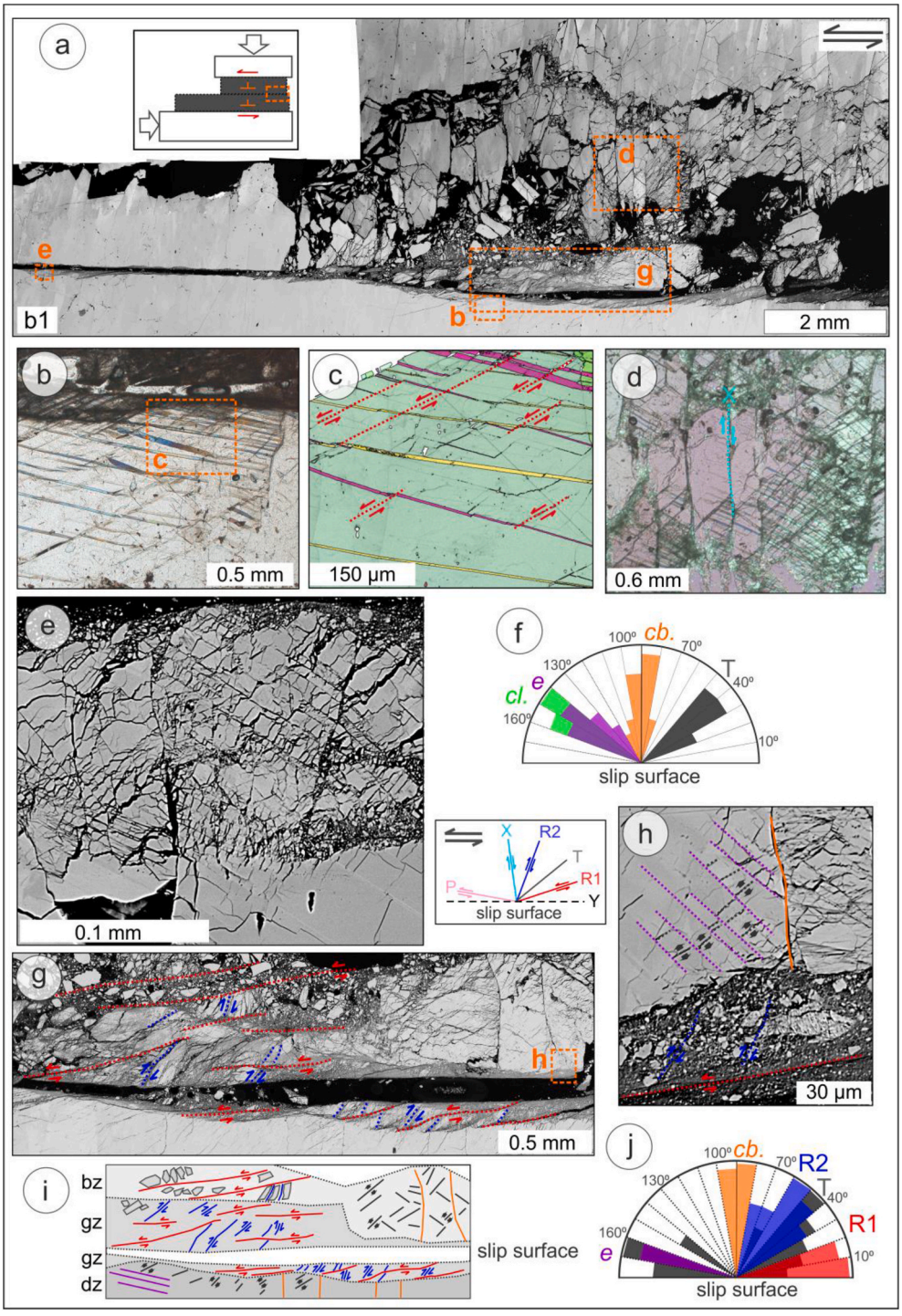

Fig. 7. Retrieved microstructures of the sample b1 (bare surface), sheared with c-axes perpendicular to the slip direction, at 1 μm/s:
a. BSE image-composite of the main deformation area, with an inset sketch of the experimental set-up and the position of the shown image; the relative, left-lateral shear sense is marked with half-arrows; the orange boxes mark the position of images (b, d, g and e); note the thicker, strain-localization area.
b. PPL micrograph shows typical damage zone, with mechanical e-twins and shear fractures; note different sets of e-twins, with varying twin thickness and intensity, that are offset by shear fractures; gouge is developed along the sliding surface (subhorizontal); the orange box marks the location of the orientation map in (c).
c. EBSD (IPF combined with image quality) map of a single calcite crystal shows two sets of twins offset by synthetic shear fractures [red] that are likely exploited as cleavage planes.
d. XPL + gypsum micrograph shows typical brecciation zone with en-echelon arrays, formed by a combination of shear and tension fractures and calcite crystal edges (subvertical), that act as antithetic X shear [cyan]; mechanical twins do not affect the whole area, only the bottom-right areas of each crystal.
e. BSE micrograph shows typical brecciation zone with in-situ pulverization and 'fanning' of the fractures: combination of sharp cleavage and zigzag fractures, likely caused by microcracking in twin lamellae (also see (h)).
f. A rose diagram of dominant orientations in brecciation zone (after d & e), with respect to the sliding surface: tension fractures [T, gray], long crystal boundaries [cb., orange], mechanical e-twins [e, purple], cleavage [cl., green]; note the overlap in twin and cleavage orientations.
g. BSE image-composite shows typical gouge zone, with fined grained material distributed by R1 and R2; the orange box shows the position of (h).
h. BSE micrograph shows microcracks [gray] inside of the twins [purple] which aided the pulverization; note well-developed Riedel shears [red R1 and blue R2] in the gouge.
i. A sketch of the typical gouge zone (after (g)) with microstructural interpretations; note the overlap in twins and tension fractures orientations; dz - damage zone, bz - brecciation zone, and gz - gouge zone; color-coding is the same as the rose diagram in Fig. 5d,g
j. A rose diagram of dominant orientations in the gouge zone (after i), with respect to the slip surface; note the relatively lower angles of R1 and tension fractures. (For interpretation of the references to color in this figure legend, the reader is referred to the Web version of this article.)

with e1, but not with the original host.

Curved twins are associated with bending of calcite crystals in the sliding direction (sinistral sense of shear), with microstructures similar to normal fault drag (undulose extinction in Fig. 5b, misorientations maps in Fig. 6e,i). Host and twin domains show strong dispersion of orientations (Fig. 6d,h). Fig. 6f,j demonstrates that the dispersion occurs around one of the a-axes, located near the center of the streonet. The dispersion is similar to the host and the twin (20–25°), and the rotation around the a-axis is counterclockwise. The misorientation profiles (Fig. 6e,i) also show up to 25° of gradual internal misorientation change along a distance of 100 μm. This is interpreted to be a result of crystal-plasticity.

Large open tension fractures that are coeval with twins, crosscut samples at ca. 60°cc-ss and break off the open edges of samples. However, on a smaller scale, tension fractures show a wide range in orientations and positions, from radial (e.g. Fig. 5f, 6a and 7e), to parallel clusters at ca. 40°cc-ss (Fig. 7f), to open micro-cracks within twin lamellae (Fig. 7h).

The *gouge zone* is dominated by fine-grained material concentrated within Riedel shears. The fine-grained material is less angular and shows evidence of grain rotation and translation. Riedel shears change their orientation as they transition from the brecciation to the gouge zone. Synthetic R1 shears first cluster at 10–20°cc-ss (Fig. 5e, j), but then coalesce with horizontal, Y-shears (Fig. 5d,g). The antithetic R2 shears cluster at 60–70°cc-ss (Fig. 5e, j), effectively bounding the lozenges in an en-echelon band structure initially (Fig. 5c and d), and later accommodating transportation of the fine-grained material.

5.2.2. *Bare surface experiments*

Bare surface experiments were set up to test the shearing mechanics of flowstone, after the setting described in Plan et al. (2010). Specimens were positioned with calcite c-axes (sub)perpendicular to the slip surface on both sides (Fig. 3c and d).

Sliding along the synthetic fault plane led to the development of isolated grooves (or toolmarks, *sensu* Stewart and Hancock, 1991) covered with fault gouge. The formation of gouge patches during slip

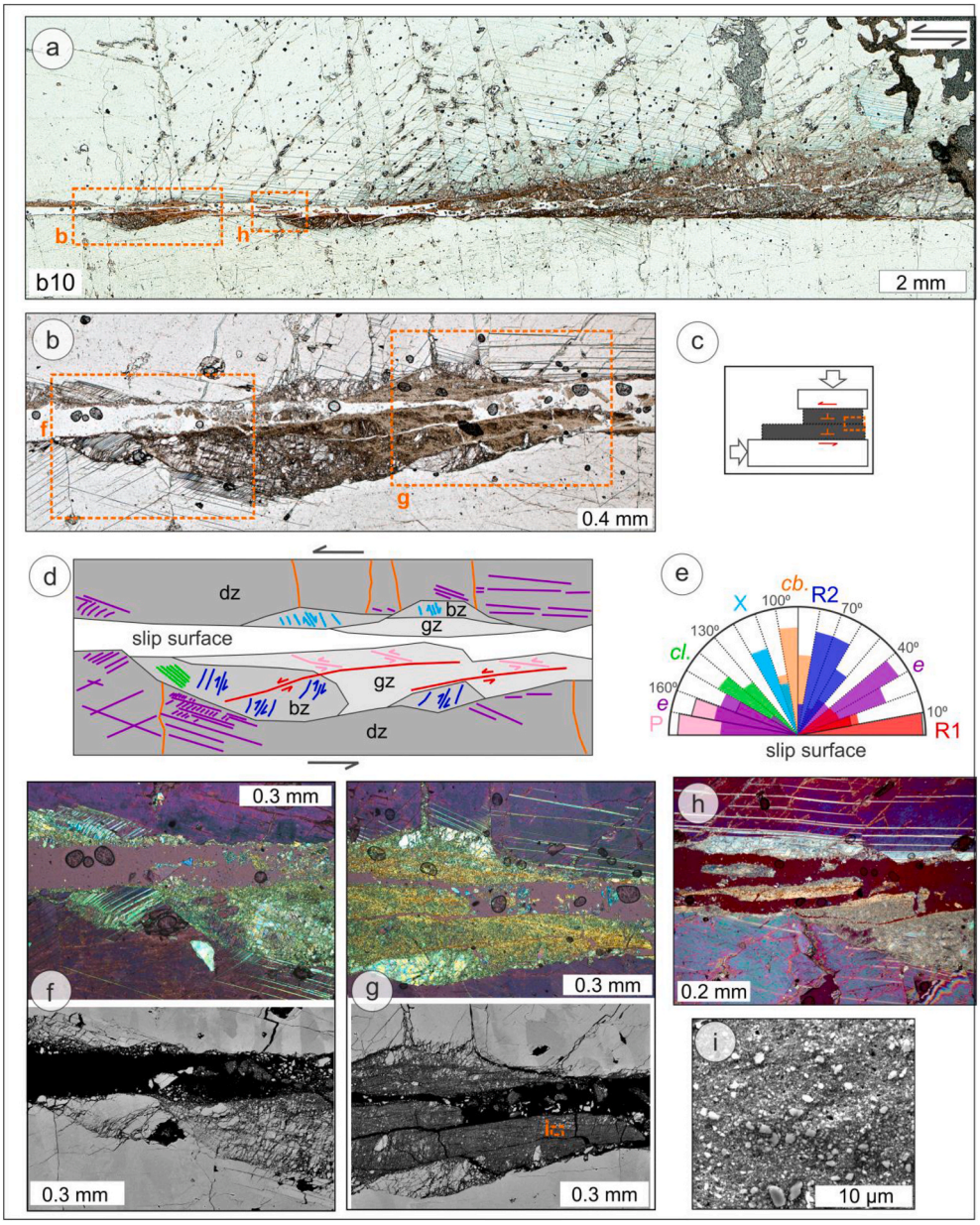

Fig. 8. Retrieved microstructures of the sample b10 (bare surface), sheared with c-axes perpendicular to the sliding direction, at 10 μm/s:
a. PPL micrograph of the main deformation area; the relative sinistral shear direction is indicated by half-arrows; the orange boxes highlight the position of images (b and h); the strain-localization area appears thinner and more finely distributed compared to sample b1.
b. PPL micrograph of typical deformation architecture with damage, brecciation and gouge zone, all overlapping; the orange boxes mark the position of images (f-g).
c. A sketch of the experimental setup and the position of the image in (a).
d. A sketch of the area in (b) with microstructural interpretations: synthetic R1 shears [red], antithetic R2 shears [blue], cleavage [cl., green], synthetic P shears [pink], antithetic X shears [cyan], mechanical e-twins [e, purple], crystal boundaries [cb., orange]; the relative sinistral shear direction is marked with half-arrows; dz - damage zone, bz - brecciation zone and gz - gouge zone.
e. A rose diagram of the dominant orientations after (d); note overall low angles of R1 shears and presence of P and X shears.
f. A pair of XPL + gypsum (upper) and BSE (lower) micrographs of the damage and brecciation zones (left side of (b)), shows in situ pulverization, caused by the interplay between brittle fracturing, twinning and micro-cracking in twins.
g. A pair of XPL + gypsum (upper) and BSE (lower) micrographs of the brecciation and gouge zones (right side of (b)), shows developing gouge in the contact of the interacting blocks; the orange box marks the position of image (i).
h. XPL + gypsum micrograph shows gouge layers with high interference colors along the slip surface.
i. SEM micrograph of the fine-grained gouge shows nanoscale material; the position is shown in Fig. 8g. (For interpretation of the references to color in this figure legend, the reader is referred to the Web version of this article.)

was accompanied by surface dilatation (A2 in Appendix), implying that parts of the original slip surfaces were not affected by subsequent slip-related deformation. Intense deformation is concentrated within a thickness of 2–3 mm from the nominal fault surface. Both samples had similar deformation modes, but b1 (sheared at 1 μm/s, Fig. 7a) is characterized by coarser fracture pattern and shorter gouge length (<2 cm) compared to b10 (at 10 μm/s, Fig. 8a), with less fractured pattern and longer gouge layer (>2 cm). The documented deformation mechanisms in bare surface experiments are twinning and fracturing, similar to intact block experiments. These processes exhibit an interplay, and transition from the damage zone to the brecciation and gouge zones (Fig. 7).

The *damage zone* is dominated by e-twins of varying orientations (Fig. 7). The most common twin set, e1, is approximately perpendicular to the loading direction, at 140–160° cc-ss (Fig. 7b–e), but clusters at ca. 30° cc-ss and 170° cc-ss also occur (Fig. 8b,e). More intense twinning is often concentrated closer to the crystal boundaries (Fig. 7b), but overall thickness and density increase closer to the sliding surface, as previously described. Twin lamellae are offset by high-angled synthetic R1 shears, aided by cleavage planes (Fig. 7c). Some twin lamellae near the principal slip zone have sets of parallel micro-tension fractures that do not extend across twin boundaries (Fig. 7h). Fig. 7d shows a slight curving of twins (bottom right corner), similar to that described for the intact setup.

The *brecciation zone* is characterized by in-situ pulverization (Fig. 7d and e). Tension fractures (at 30–50° cc-ss), and antithetic X shears (at 90° cc-ss), utilizing intercrystalline boundaries (Fig. 7d), form bookshelf or lozenge patterns. These patterns have coarser, less deformed blocks surrounded by finer material (Fig. 7d,g). Pulverization, facilitated by the interplay of tension fractures and cleavage, resulted in mosaic patterns within the shattered crystals (Fig. 7e). Cleavage orientation parallels R1 and e-twin orientations (Fig. 7e). The overall effect of in-situ pulverization is a significant reduction in grain size, transforming coarse crystals (>5 mm) into fine-grained material (<10 μm). However, in this zone, R1 and R2 shear fractures play a secondary role, forming after the main pulverization stage, when the pulverized material started translating, rotating and comminuting (Fig. 7i and 8d) to form the gouge zone.

The *gouge zone* is constituted by fine-grained material (μm-to tens of nm-size, Fig. 7g,h, 8b,f-i) localized within a 0.2 mm thick zones along the slip surface, as intricate patterns of Riedel shears (Fig. 7g), evident as light yellow bands in XPL (Fig. 8f–h). Synthetic R1 shears are typically low-angled and coalesce with P and Y shears (Fig. 7j and 8e).

6. Discussion

6.1. Progressive deformation of columnar calcite

Based on the described mechanical results and retrieved microstructures, we propose an evolutionary model of columnar calcite deformation, compare it to other similar models, and give some implications of this study, considering that, to our knowledge, this study is the first to investigate experimental shearing of columnar flowstone. The sketch of the model is shown in Fig. 9.

6.1.1. Friction vs. crystal orientation of flowstones

In single flowstone block experiments, the fracturing style directly correlates with the orientation of crystals (Fig. 9a). The sample with crystals parallel to the slip surface shows extensive fracturing, but limited strain localization and crystal plasticity. Conversely, samples with crystals perpendicular to the slip surface have high-strain domains, located either along the blocks' edges (in intact rock experiments) or along the blocks' contact (in bare rock experiments). These samples also have prominent crystal-plastic deformation (twinning and bending, Fig. 6).

The microstructures directly reflect the difference in the mechanical

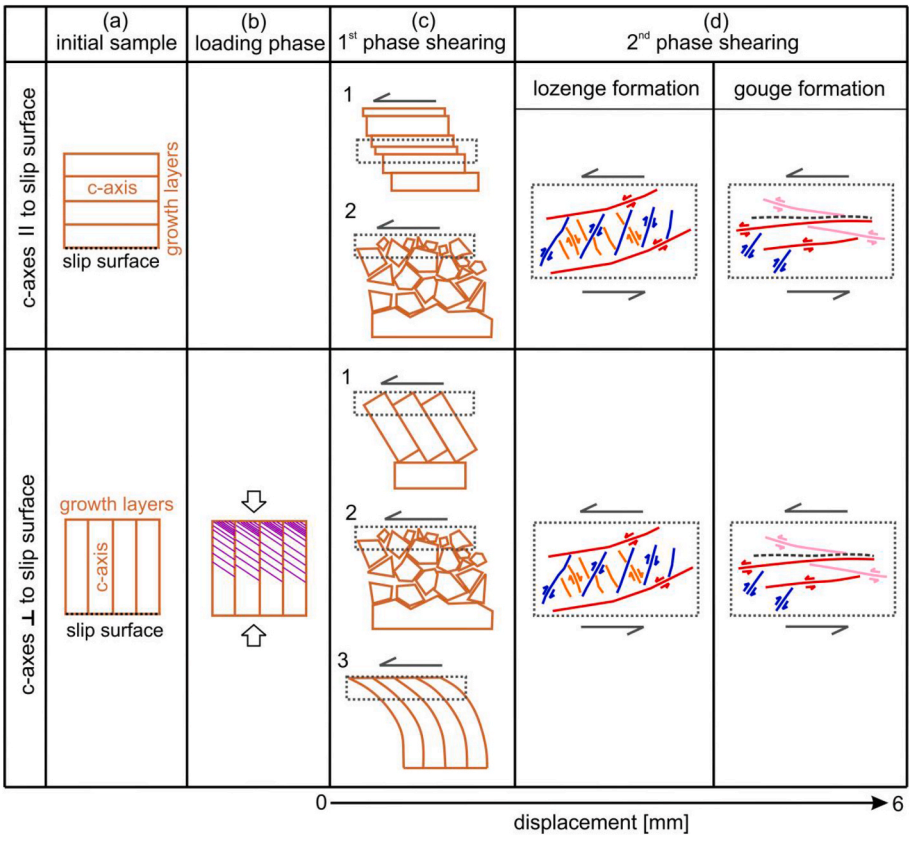

Fig. 9. Progressive deformation of columnar calcite (split in two categories, depending on the orientation of the crystals):
a. Initial sample with marked position of the calcite c-axes and growth layers, with respect to the slip surface (black dotted line).
b. Lattice distortion by mechanical twinning (only in c-axes perpendicular case, unknown for c-axes parallel case); the compression effect during the experimental loading phase is highlighted with the arrows.
c. The first phase of deformation can involve one or more shearing styles: 1. Crystal boundary activation, either as a transform shear (upper) or domino/bookshelf shear (lower), 2. In situ fracturing/brecciation with drastic grain size reduction, 3. Continuous simple shear with crystal bending; shearing styles modified after Nelson and Jones. (1987) and Ratschbacher et al. (2011); dotted rectangles mark the position of sketches in (d).
d. The second phase of deformation: lozenges formation (en-echelon R1 shear fractures linking with R2 and P-shears; P-shears exploit crystal boundaries) and gouge formation (sliding of finer material along low-angled R1-and Y- shears).

data, as seen in the friction coefficient plot (Fig. 3a). The strength of the sample with calcite crystals parallel to the sliding direction is much lower ($\mu < 0.6$), compared to the samples with perpendicular crystal orientation ($\mu > 0.7$). A lower friction coefficient suggests efficient localization and gouge production along calcite crystals, with limited jostling and fracturing of the intact rock. Conversely, a higher frictional strength of samples with perpendicular crystals probably reflects the formation of a localized slip zone at the expense of intact crystals. These crystal boundaries have poor orientation with respect to the shear direction, leading to the activation of other deformation mechanisms such as twinning and bending. A higher coefficient of friction ($0.7 < \mu < 0.95$) is also measured in experiments b1 and b10 shearing flowstones along a synthetic pre-cut fault with crystals perpendicular to the slip surface. In this case, high strength can be attributed to both (1) the development of the slip surface across poorly oriented crystals (as in the previous case) and (2) to the formation of grooves on the slip surface itself requiring additional work with respect to localization within the gouge layer. This behavior is analogous to what has been previously observed during shear of limestone synthetic faults (Tesei et al., 2017).

6.1.2. Mechanical twinning

In the samples with calcite c-axes perpendicular to the slip surface, the first deformation to appear is mechanical twinning (Fig. 9b). Since twinning in calcite is a common deformation mechanism under low grade conditions and low resolved shear stress (e.g. Burkhard 1993; De Bresser and Spiers 1997; Lacombe 2022; Rutter et al., 2022), it can develop during the loading stage of the experiments, as well as during the sliding phase. It is difficult to discriminate between twinning caused by compression (during the loading phase) and simple shear (sliding phase). However, twins accommodate a change in crystal orientation that appears together with crystal bending in the shearing direction (Fig. 5b and c and 6b) and asymmetric tensional cracks. This suggests that the effect of pure vs simple shear on mechanical twinning here is indistinguishable as it simultaneously affects crystals.

The increase in thickness and density of twin lamellae has been interpreted as an indicator of higher temperatures (Ferrill 1991; Burkhard 1993). However, there was no evidence of significant change in temperature during our experiments. Our results are similar to the recent reports of low temperature uniaxial compression of single calcite crystals and marble (Parlangeau et al., 2019, 2022). Those studies observed progressive twinning as a sequence of densification of twins, thickening of individual lamellae and merging of thickened lamellae (Lacombe 2022). Multiple twin orientations in our study (e.g. e2 in Fig. 6c,g) likely result from a combination of compression and simple shear.

Twins form complex, mutually offsetting, relationships within different twin sets and fractures, which aligns with other reports of mechanical twinning to predate and/or co-exist with other deformation mechanisms (Burkhard 1993; Demurtas et al., 2019; Lacombe 2022). However, Riedel shears mostly offset the twins, and therefore develop after the twinning.

6.1.3. Phase I: in-situ pulverization with intra- and intercrystalline deformation

The early phase of shearing includes three different mechanisms (Fig. 9c): activation of crystal boundaries (forming either bookshelf/domino or transform shear), brecciation, and continuous simple shear with crystal bending. These mechanisms have been previously presented as possible mechanisms of deformation in shear zones (Nelson and Jones 1987; Ratschbacher et al., 2011). In our samples they coincide and commingle, depending on favorable crystal orientation, and therefore, different planes of weaknesses in calcite (crystal boundaries, twins, cleavage).

(1) Activation of crystal boundaries (Figs. 9c–1): In the sample with c-axes (sub)parallel to the slip surface, active shear is transform parallel, while in samples with c-axes perpendicular to the slip surface, it has bookshelf/domino style. Existing crystal boundaries in the flowstone's columnar fabric act as planes of weakness in both scenarios. For example, the bookshelf/domino faulting is accommodated by the interplay between crystal boundaries and Riedel shears, with synthetic R1 shears forming an en-echelon structure. Antithetic X shears slide along the crystal boundaries, and together with R2, rotate domino blocks (Fig. 5c). Similar shearing styles have been described for larger scales (e.g. Wetzel et al., 1993),

(2) Brecciation (Figs. 9c–2): this mechanism involves significant grain size reduction, with very little (or no) fragment rotation and widely varying clast concentration and size (terminology after Mort and Woodcock 2008). While transgranular macroscopic fractures cut most of the samples in straight lines, chipping off sample edges, microscopic fracturing exploits a wide range of intra- and intercrystalline weaknesses, causing different processes to be active simultaneously. Splits along cleavage and twin planes result in a more regular fabric, tension fractures and microcracks within twin lamellae aid the grain size reduction, and radial and conjugate fracture sets create more chaotic fabric. Despite being associated with other mechanisms at this stage, R1 and R2 shear fractures do not have a major role in grain rotation and translation. Both cluster at higher angles with respect to the sliding surface (ca. 30° for R1 and ca. 70° for R2), indicative of general shear.

Other studies described the process of rock pulverization by dynamic rupture: pulverization is caused by the damage from stress waves originating from dynamic shear rupture tip propagation at sub-Rayleigh and/or intersonic speeds, and since a single crack cannot accommodate all the energy released, the rock is pulverized by the development of abundant microcracks (e.g. Mitchell et al., 2011; Doan and d'Hour, 2012; Schröckenfuchs et al., 2015; Fondriest et al., 2017). Dynamic rupture at the scale of the whole sample did not occur in our experiments, because our samples were sheared at subseismic velocities (<1 m/s). Instead, a combined effect of calcite breaking along the crystallographically predisposed planes of weakness, leads to the drastic grain size reduction: e.g. crystal boundaries slide along X shears, cleavage acting along R1 shears, tension cracks limited by twin lamellae. This process results in a drastic grain size reduction without significant rotation or movement of the material.

Alternatively, local high strain rates at sub-millimetric scale could have been attained in our experiments. Although the macroscopic shearing was sub-seismic, the observed stick-slip motion can be interpreted as small seismic pulses at the microscale. Stick-slip behavior, observed at shearing velocities of 10 μm/s with larger local stress drops (i10 and b10, Fig. 3), may have resulted in dynamic loading of small rock volumes near the principal slip zones (Fig. 6a and 7e). Dynamic loading at the small scale that occurs during stick-slip may also correlate with the advancement of grooves into the intact rock that are found at the holder-rock interface (Fig. 3a) or along the bare rock surfaces (Figs. 3b and 7g). Growth of grooves is akin to fracturing the intact rock within a rotated stress field (e.g. Tesei et al., 2017 and references therein), leading to simultaneous tensional and shear (via Riedel) failure at high strain rates (Fig. 7). Once formed, grooves constitute a new roughness in the fault trace, leading to a new stress concentration at their leading edge. During slow shearing, the formation of Riedel shears and/or the formation and advancement of grooves may proceed in bursts of accelerated slip and locally high strain rates. Although laboratory results are difficult to directly upscale to natural faults, pulverized rocks are supposed to form preferentially at restraining bends of fault traces (Wilson, 2005; Dor et al., 2006). In general, small scale pulverization in our experiments occurs along grooves (Fig. 7a,e,g; Fig. 5f) or due to failure of columnar crystals during jostling (Fig. 5) and/or exploiting anisotropy (Fig. 7a). Analogous to the field case, they may all

occur by stress concentration and dynamic failure at loci of restraining bends along the nominally flat experimental surfaces.

(3) Continuous simple shear with crystal bending (Figs. 9c–3): crystal bending, characterized by sinistral shear sense (Fig. 6c,g), is observed as undulatory extinction (Fig. 5b) and intracrystalline plastic deformation of up to 25° (Fig. 6e,i). Bending is prominent in the intact block experiments at higher shearing velocity (Fig. 6), while it is limited in the bare surface experiments (Fig. 7d). It is associated with twinning, where both the host and twin orientations rotate around one of the a-axes of calcite, producing a dispersion of orientations in stereonets. The lattice rotation occurs around a misorientation axis parallel to the a-axis, which plots slightly under the center of the streonet. Therefore, the misorientation axis corresponds to the kinematic rotation axis of the shear zone, similar to other reports of calcite in gouges sheared at low temperature (Bestmann and Prior 2003; Bestmann et al., 2006; Verberne et al., 2013; Pozzi et al., 2021).

6.1.4. Phase II: comminution along riedel shears

Unlike the initial stage of deformation, marked by inter- and intracrystalline deformation, in-situ pulverization, and minimal activation of Riedel shears, in the later stage of deformation, the dominant process is the movement and comminution of pulverized material along Riedel shears, with no effect of the original crystal orientation (Fig. 9d). Initial Riedel shear fractures had higher angles with respect to the sliding surface (Fig. 7d), indicative of general shear. As deformation progresses, R1 and R2 shears develop at lower angles (ca. 10° and ca. 60°, respectively, Fig. 7j,8e) to accommodate displacement and rotation of the material (Fig. 7g, 8f-h). En-echelon R1 shear fractures formed during the early phase begin to link with P shears, creating lozenges between shear fractures. This results in the production of comminuted material with finer and more rounded clasts. A new foliation develops within the fault gouge, exhibiting high interference colors (Fig. 8g and h) along the new orientations of Y and R1 shears (Fig. 7j,8e).

The formation of fault gouge appears to be almost instantaneous, with minimal movement of the broken fragments (Fig. 5b and c). The transition from coarse starting material (ca. 1 × 0.5 mm) to fully developed fault gouge containing nanoparticles (grain size <1 μm), happens within 7 mm of displacement (under dry-room conditions, low normal stress and sub seismic velocities). This process exploits pre-existing Riedel shears and capitalizes on calcite's propensity for twinning and cleavage formation, also aided by crystal boundary activation at initial stages of deformation. These observations align with the nanograin formation model (Siman-Tov et al., 2013), as it involves a combination of plastic and brittle deformation. Additionally, here described microstructures are similar to those observed in other fault gouge experiments, with developed boundary and R1 shears, both at subseismic (Verberne et al., 2013, 2014), and seismic velocities (Monzawa and Otsuki 2003; Fondriest et al., 2013; Rempe et al., 2013; Smith et al., 2015). The processes within the phase II also resemble the latter two phases of progressive fault displacement model by Billi and Storti (2004). From the original fragmentation mechanisms (corresponding to our Phase 1), change in the fragmentation mechanism is described as the ''constrained comminution'' (Sammis et al., 1987; Billi and Storti 2004), and eventually followed by further shear localization with rolling-induced particle abrasion and formation of extremely fine-grained gouge (Billi and Storti 2004).

6.2. The role of primary flowstone growth structure

The growth of calcite flowstones impacts subsequent fault-related deformation and influences the interpretation of microstructures. Flowstones consists of composite-crystals composed of individual crystallites. Growth-related undulatory extinction can be easily confused with deformation-related microstructures (Kendall and Broughton 1978). However, the absence of undulatory extinction in undeformed regions of the examined samples indicates that the undulatory extinction presented here is indeed a result of crystal bending during deformation. Similarly, twinning in fibrous calcite can be associated with growth rather than a deformation (Kendall and Tucker 1973), but the presence of twinning exclusively in strain-localized areas suggests that the described twins are deformation twins.

Interestingly, the growth layering did not affect the fracture patterns. Micritic layers often contain finer organic and clay-rich material, which may introduce impurities during deformation and/or act as a weak horizon due to low friction or poor cohesion of crystals. However, the micritic layers observed in experiments were almost unaffected by the shearing, and we found no evidence of impurities within the slip zones of our samples.

6.3. Implications

This study focuses on flowstone speleothems and contributes to further studies of active tectonics and faulting of flowstones. The research of experimental deformation of speleothems, especially flowstone, is still very limited, although multiple studies have shown that speleothems can preserve records of seismotectonic activity (e.g. Pérez-López et al., 2009; Lindgren et al., 2013; Baroň et al., 2022; Sala et al., 2022; Szczygieł et al., 2022). However, other fibrous calcites, like syn- and antitaxial veins (e.g. Kendall and Tucker 1973; Urai et al., 1991, Zhao and Li, 2022), stretched crystals or topotactic growth of calcite after high-pressure aragonites (Aravadinou et al., 2022; Gerogiannis et al., 2022) and other flowstone-like calcite fabrics (e.g. Jurewicz et al., 2007), can exhibit similar deformation mechanisms when affected by brittle faults.

Furthermore, calcite slickenfibres are common products along main fault planes and along highly strained damage zones (Stewart and Hancock, 1991; Tesei et al., 2013; Bauer et al., 2023). While there are numerous studies documenting the deformation of veins and slickenfibres during faulting at low temperature (Molli et al., 2011; Lacroix et al., 2013; Tesei et al., 2013, Marchesini et al., 2022 and many others), simultaneous studies of progressive deformation and mechanical behavior of these fault patches are rare. The deformation of fibrous calcite crystals, including twinning and tangling of dislocations as a precursor to brittle pulverization and comminution, as well as the presence of pronounced bending, has been observed in natural slickenfibres (e.g. Viti et al., 2014) and coarse calcite crystals (e.g. Kennedy and White, 2001).

In the future, it would be valuable to expand this study to include other columnar or fibrous crystals and investigate other minerals to compare their behavior with calcite. For example, experiments have been conducted on deforming columnar ice crystals (Smith and Schulson 1993, 1994; Wilson and Peternell., 2012; Wilson et al., 2014; Deng et al., 2019) and mechanical characteristics of columnar organic calcite ceramics (Wallis et al., 2022), which can provide insights into their deformation properties similar to the tests performed in this study.

7. Conclusions

We investigated the mechanics and microstructures of sheared calcite from natural flowstones, characterized by coarse crystals with distinct columnar fabric. Sliding experiments were conducted under dry-room conditions, at normal stress of 3–10 MPa and sliding velocities of 1–10 μm/s. The frictional strength of flowstone samples varied depending on the orientation of the calcite crystals, with higher strength observed when the calcite long axis was perpendicular to the sliding surface. Microstructural analysis revealed different stages of brecciation, drastic grain size reduction and rapid gouge formation with developed Riedel shears.

Key findings include the dependence of deformation patterns on flowstone's growth orientation and activation of pre-existing planes of

weakness along crystal boundaries. Early brittle deformation is comparable to brecciation stages: crackle, mosaic, chaotic. The interplay between twinning, cleavage, fractures and crystal boundary activation facilitates in-situ shattering at low shear strain. This suggests that pulverization can occur without macroscopic dynamic loading. Our microstructural analysis also emphasizes that mechanical twins are not indicative of deformation temperature, as they exhibit variations in thickness, density, and boundary curvature.

The experimental microstructures observed in flowstone offer valuable insights into fault behavior and can be applied to the evaluation of naturally faulted flowstones and other columnar microstructures.

Declaration of competing interest

The authors declare the following financial interests/personal relationships which may be considered as potential competing interests: Ivanka Mitrovic-Woodell reports financial support was provided by Austrian Science Fund. Ivo Baron reports financial support was provided by Austrian Science Fund.

Data availability

Data will be made available on request.

Acknowledgements

This research was funded by project “Active tectonics and recent dynamics of micro-displacements along major fault systems of the Eastern Alps registered in caves (SPELEOTECT)”, FWF P25884–N29 (Austrian Science Fund). We would like to thank Dr. Cristiano Collettini for allowing us to use the experimental apparatus, and Dr. Thomas Griffiths for amazing help and guidance with MTEX codes and fruitful discussions. I. Baron acknowledges the support by the Czech Science Foundation project GAČR 22–24206J and by the conceptual development project RVO 67985891 at the Institute of Rock Structure & Mechanics, Czech Academy of Sciences. We are grateful for the commitment, comments and manuscript improvements by our reviewers, Drs. Andrea Billi and Camille Parlangeau, and the editor Dr. Toru Takeshita.

Appendix A. Supplementary data

Supplementary data to this article can be found online at https://doi.org/10.1016/j.jsg.2023.104924.

References

Aravadinou, Eirini, Gerogiannis, Nikolaos, Xypolias, Paraskevas, 2022. Development and passive exhumation of high-pressure shear zones (blueschist unit, syros): insights from quartz and columnar calcite microstructures. J. Struct. Geol. 159 (June), 104607.

Bachmann, F., Hielscher, Ralf, Schaeben, Helmut, 2010. Texture analysis with MTEX – free and open source software toolbox. Solid State Phenom. 160 (February), 63–68.

Bachmann, Florian, Hielscher, Ralf, Schaeben, Helmut, 2011. Grain detection from 2d and 3d EBSD data—specification of the MTEX algorithm. Ultramicroscopy 111 (12), 1720–1733.

Balsamo, F., Storti, F., 2011. Size-dependent comminution, tectonic mixing, and sealing behavior of a ‘structurally oversimplified’ fault zone in poorly lithified sands: evidence for a coseismic rupture? GSA Bulletin 123 (3–4), 601–619.

Barber, D.J., Wenk, H.-R., 1979. Deformation twinning in calcite, dolomite, and other rhombohedral carbonates. Phys. Chem. Miner. 5 (2), 141–165.

Barber, D.J., Wenk, H.-R., Gomez-Barreiro, J., Rybacki, E., Dresen, G., 2007. Basal slip and texture development in calcite: new results from torsion experiments. Phys. Chem. Miner. 34 (2), 73–84.

Barnhoorn, Auke, Bystricky, Misha, Burlini, Luigi, Kunze, Karsten, 2004. The role of recrystallisation on the deformation behaviour of calcite rocks: large strain torsion experiments on carrara marble. J. Struct. Geol. 26 (5), 885–903.

Baroň, Ivo, Plan, Lukas, Grasemann, Bernhard, Melichar, Rostislav, Mitrović-Woodell, Ivanka, Rowberry, Matt, Scholz, Denis, 2022. Three large prehistoric earthquakes in the eastern Alps evidenced by cave rupture and speleothem damage. Geomorphology 408 (July), 108242.

Baroň, Ivo, Plan, Lukas, Sokol, Luboš, Grasemann, Bernhard, Melichar, Rostislav, Mitrovic, Ivanka, Stemberk, Josef, 2019. Present-day kinematic behaviour of active faults in the eastern Alps. Tectonophysics 752 (February), 1–23.

Bauer, Helene, Anna, Rogowitz, Habler, Gerlinde, Grasemann, Bernhard, Decker, Kurt, 2023. Interaction of frictional and plastic deformation mechanisms in a clay-carbonate strike-slip fault (northern calcareous Alps, Austria). J. Struct. Geol. 166 (January), 104774.

Bernard, Andrew B., Bradford Jensen, J., Schott, Peter K., 2006. Trade costs, firms and productivity. J. Monetary Econ. 53 (5), 917–937.

Bestmann, Michel, Kunze, Karsten, Matthews, Alan, 2000. Evolution of a calcite marble shear zone complex on thassos island, Greece: microstructural and textural fabrics and their kinematic significance. J. Struct. Geol. 22 (11), 1789–1807.

Bestmann, Michel, Prior, David J., 2003. Intragranular dynamic recrystallization in naturally deformed calcite marble: diffusion accommodated grain boundary sliding as a result of subgrain rotation recrystallization. J. Struct. Geol. 25 (10), 1597–1613.

Bestmann, Michel, Prior, David J., Grasemann, Bernhard, 2006. Characterisation of deformation and flow mechanics around porphyroclasts in a calcite marble ultramylonite by means of EBSD analysis. Tectonophysics 413 (3–4), 185–200. https://doi.org/10.1016/j.tecto.2005.10.044. ISSN 0040-1951.

Billi, Andrea, 2005. Grain size distribution and thickness of breccia and gouge zones from thin (<1m) strike-slip fault cores in limestone. J. Struct. Geol. 27 (10), 1823–1837.

Billi, Andrea, Storti, Fabrizio, 2004. Fractal distribution of particle size in carbonate cataclastic rocks from the core of a regional strike-slip fault zone. Tectonophysics 384 (1), 115–128.

Braillon, P., Kubin, L., Serughetti, J., 1978. Plastic deformation of calcite single crystals deformed in compression parallel to [111]. Phys. Status Solidi: Applied Research 45 (2), 453–462.

Bresser, J. H. P. de, Spiers, C.J., 1993. Slip systems in calcite single crystals deformed at 300-800°C. J. Geophys. Res. 98 (B4), 6397–6409.

Broughton, Paul L., 1983. Environmental implications of competitive growth fabrics in stalactitic carbonate. Int. J. Speleol./Societa Speleologica Italiana 13 (1), 3.

Burchfiel, B.C., Royden, L.H., Van der Hilst, R.D., Hager, B.H., Chen, Z., King, R.W., Li, C., Lü, J., Yao, H., Kirby, E., 2008. A geological and geophysical context for the wenchuan earthquake of 12 may 2008, sichuan, people’s Republic of China. GSA Today (Geol. Soc. Am.): A Publication of the Geological Society of America 18 (7), 4–11.

Burkhard, Martin, 1993. Calcite twins, their geometry, appearance and significance as stress-strain markers and indicators of tectonic regime: a review. J. Struct. Geol. 15 (3–5), 351–368.

Chiaraluce, L., Barchi, M., Collettini, C., Mirabella, F., 2005. Connecting seismically active normal faults with quaternary geological structures in a complex extensional environment: the colfiorito 1997 case history (northern …. https://doi.org/10.1029/2004TC001627.

Chiaraluce, L., Di Stefano, R., Tinti, E., Scognamiglio, L., Michele, M., Casarotti, E., Cattaneo, M., et al., 2017. The 2016 Central Italy seismic sequence: a first look at the mainshocks, aftershocks, and source models. Seismol Res. Lett. 88 (3), 757–771.

Collettini, Cristiano, Stefano, Giuseppe Di, Carpenter, Brett, Scarlato, Piergiorgio, Tesei, Telemaco, Mollo, Silvio, Trippetta, Fabio, Marone, Chris, Romeo, Gianni, Chiaraluce, Lauro, 2014. A novel and versatile apparatus for brittle rock deformation. Int. J. Rock Mech. Min. Sci. 66 (February), 114–123.

De Bresser, J.H.P., Spiers, C.J., 1997. Strength characteristics of the R, F, and c slip systems in calcite. Tectonophysics 272 (1), 1–23.

Demurtas, Matteo, Smith, Steven A.F., Prior, David J., Spagnuolo, Elena, Di Toro, Giulio, 2019. Development of crystallographic preferred orientation during cataclasis in low-temperature carbonate fault gouge. J. Struct. Geol. 126 (September), 37–50.

Deng, Yu, Li, Zongkun, Li, Zhijun, Wang, Juan, 2019. The experiment of fracture mechanics characteristics of yellow river ice. Cold Reg. Sci. Technol. 168 (December), 102896.

De Paola, Nicola, Holdsworth, Robert E., Viti, Cecilia, Collettini, Cristiano, Bullock, Rachael, 2015. Can grain size sensitive flow lubricate faults during the initial stages of earthquake propagation? Earth Planet Sci. Lett. 431 (December), 48–58.

Dickson, J.A.D., 1993. Inorganic calcite morphology: roles of fluid chemistry and fluid flow: discussion. J. Sediment. Res. 63 (3). https://archives.datapages.com/data/sepm/journals/v63-66/data/063/063003/0560.htm.

Doan, Mai-Linh, Gary, Gérard, 2009. Rock pulverization at high strain rate near the san andreas fault. Nat. Geosci. 2 (10), 709–712.

Doan, Mai-Linh, d’Hour, Virginie, 2012. Effect of initial damage on rock pulverization along faults. J. Struct. Geol. 45 (December), 113–124.

Dor, Ory, Ben-Zion, Yehuda, Rockwell, Thomas K., Jim Brune, 2006. Pulverized rocks in the mojave section of the san andreas fault zone. Earth Planet Sci. Lett. 245 (3), 642–654.

Fairchild, Ian J., Smith, Claire L., Baker, Andy, Fuller, Lisa, Spötl, Christoph, Mattey, Dave, McDermott, Frank, M.F, E.I., 2006. Modification and preservation of environmental signals in speleothems. Earth Sci. Rev. 75 (1), 105–153.

Ferrill, David A., 1991. Calcite twin widths and intensities as metamorphic indicators in natural low-temperature deformation of limestone. J. Struct. Geol. 13 (6), 667–675.

Fondriest, Michele, Aretusini, Stefano, Di Toro, Giulio, Steven, A., Smith, F., 2015. Fracturing and rock pulverization along an exhumed seismogenic fault zone in dolostones: the foiana fault zone (southern Alps, Italy). Tectonophysics 654 (July), 56–74.

Fondriest, Michele, Doan, Mai-Linh, Aben, Frans, Fusseis, Florian, Mitchell, Thomas M., Voorn, Maarten, Secco, Michele, Di Toro, Giulio, 2017. Static versus dynamic fracturing in shallow carbonate fault zones. Earth Planet Sci. Lett. 461 (March), 8–19.

Fondriest, Michele, Smith, Steven A.F., Candela, Thibault, Nielsen, Stefan B., Mair, Karen, Di Toro, Giulio, 2013. Mirror-like faults and power dissipation during earthquakes. Geology 41 (11), 1175–1178.
Fondriest, Michele, Smith, Steven A.F., Di Toro, Giulio, Zampieri, Dario, Mittempergher, Silvia, 2012. Fault zone structure and seismic slip localization in dolostones, an example from the southern Alps, Italy. J. Struct. Geol. 45 (December), 52–67.
Freund, L.B., 1998. Dynamic Fracture Mechanics. Cambridge University Press.
Frisia, Silvia, 2014. Microstratigraphic logging of calcite fabrics in speleothems as tool for palaeoclimate studies. Int. J. Speleol./Societa Speleologica Italiana 44 (1), 1.
Frisia, Silvia, Borsato, Andrea, Fairchild, Ian J., McDermott, Frank, 2000. Calcite fabrics, growth mechanisms, and environments of formation in speleothems from the Italian Alps and southwestern Ireland. J. Sediment. Res. 70 (5), 1183–1196.
Gerogiannis, Nikolaos, Chatzaras, Vasileios, Aravadinou, Eirini, Gürer, Derya, Xypolias, Paraskevas, 2022. Microstructural and textural modification of columnar calcite under increasing shear strain (evia island, Greece). J. Struct. Geol. 160 (July), 104632.
Healy, David, Rizzo, Roberto E., Cornwell, David G., Farrell, Natalie J.C., Watkins, Hannah, Timms, Nick E., Gomez-Rivas, Enrique, Smith, Michael, 2017. FracPaQ: a MATLABTM toolbox for the quantification of fracture patterns. J. Struct. Geol. 95 (February), 1–16.
Jurewicz, Edyta, Hercman, Helena, Nejbert, Krzysztof, 2007. Flowstone-like calcite in the andesite of jarmuta Mt. – dating the holocene tectonic activity in the vicinity of szczawnica (magura nappe, outer carpathians, Poland). Acta Geol. Pol. 57 (2), 187–204.
Kendall, A.C., Tucker, M.E., 1973. Radiaxial fibrous calcite: a replacement after acicular carbonate. Sedimentology 20 (3), 365–389.
Kendall, Alan C., Broughton, Paul L., 1978. Origin of fabrics in speleothems composed of columnar calcite crystals. J. Sediment. Res. 48 (2), 519–538.
Kennedy, L.A., White, J.C., 2001. Low-temperature recrystallization in calcite: mechanisms and consequences. Geology 29 (11), 1027.
Lacombe, Olivier, 2022. Calcite deformation twins: from crystal plasticity to applications in geosciences. Geosci. J. 12 (7), 280.
Lacroix, B., Leclère, H., Buatier, M., Fabbri, O., 2013. Weakening processes in thrust faults: insights from the monte perdido thrust fault (southern pyrenees, Spain). Geofluids 13 (1), 56–65.
Lindgren, Paula, Price, Mark C., Lee, Martin R., Burchell, Mark J., 2013. Constraining the pressure threshold of impact induced calcite twinning: implications for the deformation history of aqueously altered carbonaceous chondrite parent bodies. Earth Planet Sci. Lett. 384 (December), 71–80.
Linzer, Hans-Gert, Decker, Kurt, Peresson, Herwig, Dell'Mour, Rudi, Frisch, Wolfgang, 2002. Balancing lateral orogenic float of the eastern Alps. Tectonophysics 354 (3), 211–237.
Logan, J.M., Friedman, M., Higgs, N., Dengo, C., 1979. Experimental studies of simulated gouge and their application to studies of natural fault zones. US Geol. Surv. Open-File Report 79–1239.
Luther, Amy, Gary, Axen, Jane, Selverstone, 2013. Particle-size distributions of low-angle normal fault breccias: implications for slip mechanisms on weak faults. J. Struct. Geol. 55 (October), 50–61.
Mair, K., Abe, S., 2011. Breaking up: comminution mechanisms in sheared simulated fault gouge. Pure Appl. Geophys. 168 (12), 2277–2288.
Marchesini, Barbara, Eugenio, Carminati, Aldega, Luca, Francesco, Mirabella, Maurizio, Petrelli, Antonio, Caracausi, Barchi, Massimiliano R., 2022. Chemical interaction driven by deep fluids in the damage zone of a seismogenic carbonate fault. J. Struct. Geol. 161, 104668. https://doi.org/10.1016/j.jsg.2022.104668. ISSN 0191-8141.
Mitchell, T.M., Ben-Zion, Y., Shimamoto, T., 2011. Pulverized Fault rocks and damage asymmetry along the arima-takatsuki tectonic line, Japan. Earth Planet Sci. Lett. 308 (3), 284–297.
Molli, Giancarlo, White, Joseph Clancy, Kennedy, Lori, Taini, Veronica, 2011. Low-temperature deformation of limestone, isola palmaria, northern apennine, Italy – the role of primary textures, precursory veins and intracrystalline deformation in localization. J. Struct. Geol. 33 (3), 255–270.
Monzawa, Nobuaki, Otsuki, Kenshiro, 2003. Comminution and fluidization of granular fault materials: implications for fault slip behavior. Tectonophysics 367 (1), 127–143.
Mort, K., Woodcock, N.H., 2008. Quantifying Fault breccia geometry: dent fault, NW england. J. Struct. Geol. 30 (6), 701–709.
Nelson, Michael R., Jones, Craig H., 1987. Paleomagnetism and crustal rotations along a shear zone, las vegas range, southern Nevada. Tectonics 6 (1), 13–33.
Niemeijer, André, Di Toro, Giulio, Griffith, W. Ashley, Bistacchi, Andrea, Steven, A., Smith, F., Nielsen, Stefan, 2012. Inferring earthquake physics and chemistry using an integrated field and laboratory approach. J. Struct. Geol. 39 (June), 2–36.
Nolze, G., Hielscher, R., 2016. Orientations – perfectly colored. J. Appl. Crystallogr. 49 (5), 1786–1802.
Parlangeau, Camille, Alexandre, Dimanov, Hallais, Simon, 2022. In-situ evolution of calcite twinning during uniaxial compression of carrara marble at room temperature. Geosci. J. 12 (6), 233.
Parlangeau, Camille, Alexandre, Dimanov, Lacombe, Olivier, Hallais, Simon, Daniel, Jean-Marc, 2019. Uniaxial compression of calcite single crystals at room temperature: insights into twinning activation and development. Solid Earth 10 (1), 307–316.
Pérez-López, R., Rodríguez-Pascua, M.A., Giner-Robles, J.L., Martínez-Díaz, J.J., Marcos-Nuez, A., Silva, P.G., Bejar, M., Calvo, J.P., 2009. Speleoseismology and palaeoseismicity of benis cave (murcia, SE Spain): coseismic effects of the 1999 mula earthquake (mb 4.8). Geological Society, London, Special Publications 316 (1), 207–216.
Plan, Lukas, Grasemann, Bernhard, Spötl, Christoph, Decker, Kurt, Boch, Ronny, Kramers, Jan, 2010. Neotectonic extrusion of the eastern Alps: constraints from U/Th dating of tectonically damaged speleothems. Geology 38 (6), 483–486.
Plan, Lukas, Spötl, Christoph, Bryda, Gerhard, 2019. Speläologie und geologie der hirschgrubenhöhle Am Hochschwab (steiermark). Hohle 70 (1–4), 79–93.
Pozzi, Giacomo, De Paola, Nicola, Nielsen, Stefan B., Holdsworth, Robert E., Tesei, Telemaco, Thieme, Manuel, Demouchy, Sylvie, 2021. Coseismic Fault lubrication by viscous deformation. Nat. Geosci. 14 (6), 437–442.
Ratschbacher, L., Krumrei, I., Blumenwitz, M., Staiger, M., Appel, E., 2011. Rifting and strike-slip shear in central tibet and the geometry, age and kinematics of upper crustal extension in tibet. Geological Society London Special Publications 153 (1), 127–163.
Reches, Ze 'ev, Dewers, Thomas A., 2005. Gouge Formation by dynamic pulverization during earthquake rupture. Earth Planet Sci. Lett. 235 (1), 361–374.
Reches, Ze 'ev, Lockner, David A., 2010. Fault weakening and earthquake instability by powder lubrication. Nature 467 (7314), 452–455.
Ree, Jin-Han, Ando, Jun-Ichi, Han, Raehee, Shimamoto, Toshihiko, 2014. Coseismic microstructures of experimental fault zones in carrara marble. J. Struct. Geol. 66 (September), 75–83.
Rempe, Marieke, Mitchell, Thomas, Renner, Jörg, Nippress, Stuart, Ben-Zion, Yehuda, Rockwell, Thomas, 2013. Damage and seismic velocity structure of pulverized rocks near the san andreas fault. J. Geophys. Res. Solid Earth 118 (6), 2813–2831.
Rutter, Ernest, Wallis, David, Kosiorek, Kamil, 2022. Application of electron backscatter diffraction to calcite-twinning paleopiezometry. Geosci. J. 12 (6), 222.
Rybacki, E., Janssen, C., Wirth, R., Chen, K., Wenk, H.-R., Stromeyer, D., Dresen, G., 2011. Low-temperature deformation in calcite veins of SAFOD core samples (san andreas fault) — microstructural analysis and implications for fault rheology. Tectonophysics 509 (1), 107–119.
Sala, Przemysław, Bella, Pavel, Szczygieł, Jacek, Wróblewski, Wojciech, Gradziński, Michał, 2022. Healed speleothems: a possible indicator of seismotectonic activity in karst areas. Sediment. Geol. 430 (March), 106105.
Sammis, Charles, King, Geoffrey, Biegel, Ronald, 1987. The kinematics of gouge deformation. Pure Appl. Geophys. 125 (5), 777–812.
Schröckenfuchs, Theresa, Bauer, Helene, Grasemann, Bernhard, Decker, Kurt, 2015. Rock pulverization and localization of a strike-slip fault zone in dolomite rocks (Salzach–Ennstal–Mariazell–Puchberg fault, Austria). J. Struct. Geol. 78 (September), 67–85.
Siman-Tov, Shalev, Aharonov, Einat, Sagy, Amir, Emmanuel, Simon, 2013. Nanograins form carbonate fault mirrors. Geology 41 (6), 703–706.
Smith, S.A.F., Billi, A., Toro, G.D., et al., 2011. Principal Slip Zones in Limestone: Microstructural Characterization and Implications for the Seismic Cycle (Tre Monti Fault, Central Apennines, Italy). Pure Appl. Geophys. 168, 2365–2393. https://doi.org/10.1007/s00024-011-0267-5.
Smith, S.A.F., Nielsen, S., Di Toro, G., 2015. Strain localization and the onset of dynamic weakening in calcite fault gouge. Earth Planet Sci. Lett. 413 (March), 25–36.
Smith, T.R., Schulson, E.M., 1993. The brittle compressive failure of fresh-water columnar ice under biaxial loading. Acta Metall. Mater. 41 (1), 153–163.
Smith, T.R., Schulson, E.M., 1994. Brittle compressive failure of salt-water columnar ice under biaxial loading. J. Glaciol. 40 (135), 265–276.
Stewart, I.S., Hancock, P.L., 1991. Scales of structural heterogeneity within neotectonic normal fault zones in the aegean region. J. Struct. Geol. 13 (2), 191–204.
Storti, Fabrizio, Billi, Andrea, Salvini, Francesco, 2003. Particle size distributions in natural carbonate fault rocks: insights for non-self-similar cataclasis. Earth Planet Sci. Lett. 206 (1–2), 173–186.
Szczygieł, Jacek, Baroň, Ivo, Melichar, Rostislav, Plan, Lukas, Mitrović-Woodell, Ivanka, Kaminsky, Eva, Scholz, Denis, Grasemann, Bernhard, 2022. Post-miocene tectonics of the northern calcareous Alps. Sci. Rep. 12 (1), 17730.
Tesei, Telemaco, Carpenter, Brett M., Giorgetti, Carolina, Scuderi, Marco M., Sagy, Amir, Scarlato, Piergiorgio, Collettini, Cristiano, 2017. Friction and scale-dependent deformation processes of large experimental carbonate faults. J. Struct. Geol. 100 (July), 12–23.
Tesei, Telemaco, Collettini, Cristiano, Barchi, Massimiliano R., Carpenter, Brett M., Stefano, Giuseppe Di, 2014. Heterogeneous strength and fault zone complexity of carbonate-bearing thrusts with possible implications for seismicity. Earth Planet Sci. Lett. 408 (December), 307–318.
Tesei, Telemaco, Collettini, Cristiano, Viti, Cecilia, Barchi, Massimiliano R., 2013. "Fault architecture and deformation mechanisms in exhumed analogues of seismogenic carbonate-bearing thrusts.". J. Struct. Geol. 55 (October), 167–181.
Turner, Francis J., Orozco, Miguel, 1976. "Crystal bending in metamorphic calcite, and its relations to associated twinning." contributions to mineralogy and petrology. Beitrage Zur Mineralogie Und Petrologie 57 (1), 83–97.
Urai, J.L., Williams, P.F., van Roermund, H.L.M., 1991. Kinematics of crystal growth in syntectonic fibrous veins. J. Struct. Geol. 13 (7), 823–836.
Verberne, B.A., Spiers, C.J., Niemeijer, A.R., De Bresser, J.H.P., De Winter, D.A.M., Plümper, O., 2014. Frictional properties and microstructure of calcite-rich fault gouges sheared at sub-seismic sliding velocities. Pure Appl. Geophys. 171 (10), 2617–2640.
Verberne, Berend A., de Bresser, Johannes H.P., André, R., Niemeijer, Christopher J., Spiers, D.A., de Winter, Matthijs, Oliver, Plümper, 2013. Nanocrystalline slip zones in calcite fault gouge show intense crystallographic preferred orientation: crystal plasticity at sub-seismic slip rates at 18–150 °C. Geology 41 (8), 863–866.
Viti, C., Collettini, C., Tesei, T., 2014. "Pressure solution seams in carbonatic fault rocks: mineralogy, micro/nanostructures and deformation mechanism." contributions to mineralogy and petrology. Beitrage Zur Mineralogie Und Petrologie 167 (2), 970.

Wallis, David, Harris, Joe, Böhm, Corinna F., Wang, Di, Zavattieri, Pablo, Feldner, Patrick, Merle, Benoit, et al., 2022. Progressive changes in crystallographic textures of biominerals generate functionally graded ceramics. Materials Advances 3 (3), 1527–1538.

Wetzel, Laura Reiser, Wiens, Douglas A., Kleinrock, Martin C., 1993. Evidence from earthquake for bookshelf faulting at large non-transform ridge offsets. Nature 362 (6417). https://doi.org/10.1038/362235a0.

Wilson, Brent, Dewers, Thomas, 'ev Reches, Ze, Brune, James, 2005. Particle size and energetics of gouge from earthquake rupture zones. Nature 434 (7034), 749–752.

Wilson, Christopher J.L., Peternell, Mark, 2012. Ice deformed in compression and simple shear: control of temperature and initial fabric. J. Glaciol. 58 (207), 11–22.

Wilson, Christopher J.L., Peternell, Mark, Piazolo, Sandra, Luzin, Vladimir, 2014. Microstructure and fabric development in ice: lessons learned from in situ experiments and implications for understanding rock evolution. J. Struct. Geol. 61 (April), 50–77.

Yuan, Fuping, Prakash, Vikas, Terry, Tullis, 2011. Origin of pulverized rocks during earthquake fault rupture. J. Geophys. Res. 116 (B6) https://doi.org/10.1029/2010jb007721.

Zhao, Bangsheng, Li, Rongxi, 2022. Formation mechanism of bedding-parallel antitaxial fibrous veins in shale: A review. J. Struct. Geol. 161, 104653. https://doi.org/10.1016/j.jsg.2022.104653. ISSN 0191-8141.